JOURNAL OF GEOPHYSICAL RESEARCH, VOL. 106, NO. 12, PAGES 30645–30670, DECEMBER 10, 2001

Crustal and upper mantle structure beneath Antarctica and surrounding oceans

Michael H. Ritzwoller, Nikolai M. Shapiro, Anatoli L. Levshin, and Garrett M. Leahy
Center for Imaging the Earth's Interior, Department of Physics, University of Colorado, Boulder, Colorado, USA

Abstract. We present and discuss a new model of the crust and upper mantle at high southern latitudes that is produced from a large, new data set of fundamental mode surface wave dispersion measurements. The inversion for a $2^\circ \times 2^\circ$ shear velocity model breaks into two principal steps: first, surface wave tomography in which dispersion maps are produced for a discrete set of periods for each wave type (Rayleigh group velocity, 18–175 s; Love group velocity, 20–150 s; Rayleigh and Love phase velocity, 40–150 s) and, second, inversion for a shear velocity model. In the first step, we estimate average resolution at high southern latitudes to be about 600 km for Rayleigh waves and 700 km for Love waves. The second step is a multistage process that culminates in a Monte Carlo inversion yielding an ensemble of acceptable models at each spatial node. The middle of the ensemble (median model) together with the half width of the corridor defined by the ensemble summarize the results of the inversion. The median model fits the dispersion maps at about the measurement error (group velocities, 20–25 m/s; phase velocities, 10–15 m/s) and the dispersion data themselves at about twice the measurement error. We refer to the features that appear in every member of the ensemble as "persistent." Some of persistent features are the following: (1) Crustal thickness averages ~27 km in West Antarctica and ~40 km in East Antarctica, with maximum thicknesses approaching 45 km. (2) Although the East Antarctic craton displays variations in both maximum velocity and thickness, it appears to be a more or less average craton. (3) The upper mantle beneath much of West Antarctica is slow and beneath the West Antarctic Rift is nearly indistinguishable from currently dormant extensional regions such as the western Mediterranean and the Sea of Japan. Our model is therefore consistent with evidence of active volcanism underlying the West Antarctic ice sheet, and we hypothesize that the West Antarctic Rift is the remnant of events of lithospheric rejuvenation in the recent past that are now quiescent. (4) The Australian-Antarctic Discordance is characterized by a moderately high velocity lid to a depth of 70–80 km with low velocities wrapping around the discordance to the south. There is a weak trend of relatively high velocities dipping to the west at greater depths that requires further concentrated efforts to resolve. (5) The strength of radial anisotropy $(v_{sh} - v_{sv})/v_{sv}$ in the uppermost mantle across the Southern Hemisphere averages ~4%, similar to the Preliminary Reference Earth Model. Radial anisotropy appears to be slightly stronger in West Antarctica than in East Antarctica and in the thinner rather than the thicker regions of the East Antarctic craton.

1. Introduction

The crust and lithosphere beneath Antarctica are among the most poorly understood regions directly underlying Earth's surface. This results partially from the obvious fact that Antarctic ice sheets insulate geologists from direct crustal observation, but it is also related to the difficulty and expense of acquiring high-quality well-distributed seismic information across the continent. Controlled source seismic experiments (long baseline refraction and reflection profiles) have provided fairly localized (although very important) two-dimensional (2-D) images [e.g., *Kogan*, 1972; *Ito and Ikami*, 1986]. Passive source seismology has yielded neither the quantity nor the quality of information that has been revealed about the substructure of other continents. Except for a few locations, permanent seismic stations have proven difficult to maintain especially at ice sites, and because intraplate seismicity within the Antarctic Plate is rare [*Okal*, 1981], passive studies have and will continue to rely predominantly on the use of earthquakes no closer than the Antarctic Plate margin. Consequently, teleseismic body wave studies have provided only a few localized structural constraints and surface wave studies have displayed poor, although recently improving [e.g., *Roult et al.*, 1994; *Vdovin*, 1999; *Danesi and Morelli*, 2000], radial and lateral resolutions. There has been a recent international resurgence of interest in the continental crust [e.g., *Meissner*, 1986; *Christensen and Mooney*, 1995], but the above mentioned factors have meant that Antarctica has not yet played a particularly significant role in these investigations. This is unfortunate, not only due to interest in the intrinsic composition and development of the Antarctic Plate but also because of Antarctica's strategic location in models of Phanerozoic continental evolution.

In this paper, we report the results of a study designed to improve information about the shear velocity structure beneath Antarctica and surrounding regions in order to provide constraints on thermal and chemical variations, particularly in the uppermost mantle. We present a new model of the crust and upper mantle beneath this region produced from a large, new data set of fundamental mode surface wave dispersion measurements. The use of surface wave data to constrain mantle structure at high southern latitudes helps to circumvent problems created by the relative paucity of receiving stations on the Antarctic continent

Paper number 2001JB000179.
0148-0227/01/2001JB000179$09.00

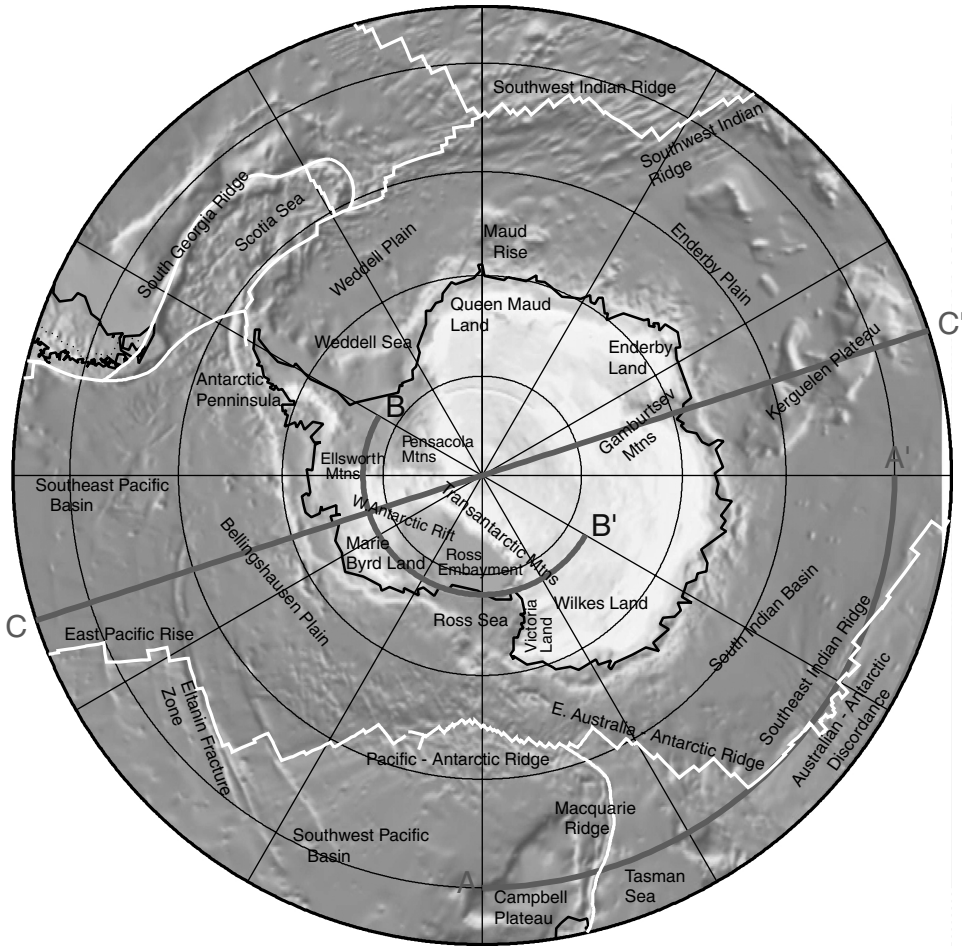

Figure 1. Index map of Antarctica and surroundings showing some of the features discussed in the text. The lines A-A′, B-B′, C-C′ indicate the depth profiles shown in Plate 5.

and the shortage of intraplate seismicity across the Antarctic Plate. For this reason, there is a long history of surface wave studies of Antarctica [e.g., *Evison*, 1963; *Evison et al.*, 1960; *Kovach and Press*, 1961; *Bentley and Ostenso*, 1962; *Dewart and Toksoz*, 1965; *Knopoff and Vane*, 1978; *Neunhofer et al.*, 1983; *Rouland et al.*, 1985; *Forsyth et al.*, 1987; *Montagner and Jobert*, 1988; *Grad et al.*, 1993; *Roult et al.*, 1994; *Bannister et al.*, 2000]. *Roult and Rouland* [1994] present an excellent review. Only recently, however, have sufficient broadband seismic data accumulated to the point that surface wave tomography can yield relatively high resolution images across much of the region of study (Figure 1).

The data that we use come from two sources. First, phase velocity measurements at intermediate and long periods (40–150 s) were graciously donated to this study by scientists at Harvard University and Utrecht University. Second, we also use a new compilation of group velocity measurements that extends to much shorter periods (~20 s). N. M. Shapiro and M. H. Ritzwoller (Monte-Carlo inversion of broad-band surface wave dispersion for a global shear velocity model of the crust and upper mantle, submitted to *Geophysical Journal International*, 2001, hereinafter referred to as SR2001) show that the simultaneous inversion of broadband group and phase velocity data in the presence of a priori constraints on allowable structures in the crust and upper mantle ameliorates the trade-off between crustal and upper mantle structures that plague inversions of surface waves in continental areas. In oceanic regions it improves abilities to resolve the lithosphere from the asthenosphere. The result is a significantly improved model of the uppermost mantle.

We divide the inverse problem for a shear velocity model of the crust and upper mantle to a depth of ~400 km into two principal steps. The first step is surface wave tomography in which surface wave dispersion measurements are used to infer dispersion maps on a discrete grid of periods for both Rayleigh and Love waves. The second step is the use of these maps as data to invert for a shear velocity model of the crust and upper mantle. At each point, we invert four dispersion curves, one each for Rayleigh and Love wave group and phase velocity. The methods of tomographic imaging [*Barmin et al.*, 2001] (hereinafter referred to as BRL2001) and subsequent inversion for a shear velocity model (SR2001) are designed to be used together to provide consistent perturbations that revert to an initial model in regions of poor data coverage. As initial models, in the crust we use CRUST5.1 [*Mooney et al.*, 1998], and in the mantle we use the isotropic version of model S20A [*Ekstrom et al.*, 1997] modified to match the radial anisotropy in Preliminary Reference Earth Model (PREM) [*Dziewonski and Anderson*, 1981]. As Figure 2 shows, the ice sheets of Antarctica strongly affect surface wave velocities at short and intermediate periods, and the initial model must contain realistic ice thicknesses and velocities.

A principal component of the inversion method of SR2001 is the production of an ensemble of models that fit the data acceptably at every geographical point. The most robust features of the resulting model are those that appear in every acceptable model. SR2001 refer to these features as "persis-

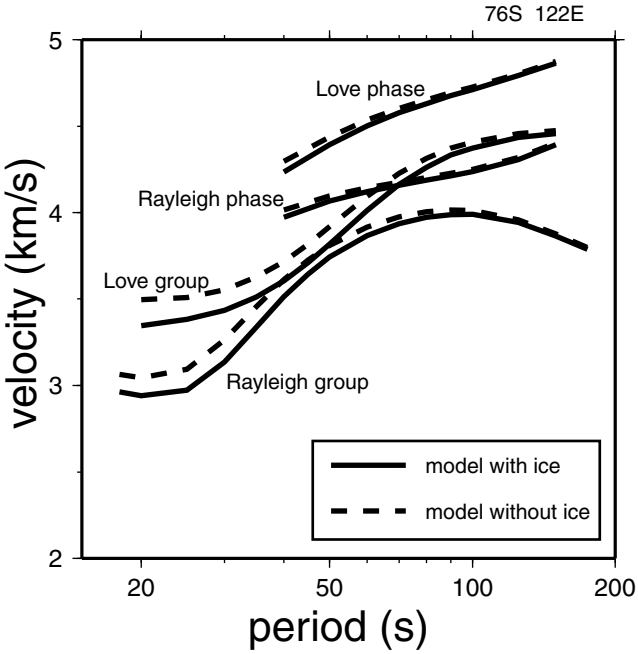

Figure 2. Demonstration of the effect of an ice sheet on surface wave velocities. Solid lines are the group and phase velocities predicted from the median model, described below, for a point in East Antarctica (76°S, 122°E) with an ice thickness of ~3.8 km. The dispersion curves for the same model without the ice are the dashed lines. The thickening of the "crust" by the ice sheet reduces the surface wave velocities at intermediate periods, and the ice itself reduces the velocities at short periods much as a sedimentary basin would. The *P* and *S* velocities of the ice, however, are faster than shallow sediments, and the low surface wave velocities at short periods result dominantly from the very low density of ice.

tent." We will concentrate discussion on the persistent features of the model.

In this paper, we attempt to summarize the main results of our study of Antarctica and the surrounding oceans; from data acquisition and processing (section 2), to inversion methodology (section 3), and to a preliminary discussion of the persistent features that appear in the shear velocity model of the crust and upper mantle (section 4). Space prohibits an exhaustive discussion of the all of the steps that lead to the model. For further information about the data processing, the reader should see *Ritzwoller and Levshin* [1998] (hereinafter referred to as RL1998), BRL2001 provide a more complete discussion of the method of surface wave tomography and resolution analysis, and SR2001 give a fuller description of the method of inversion for a shear velocity model of the crust and uppermost mantle. This paper is an application of methods largely described elsewhere, and we will attempt to point to some of the more intriguing features of the crust and upper mantle that have emerged in this study.

2. Data

The data are surface wave group and phase velocity measurements. We measured group velocities using the method documented by RL1998. This is a frequency-time method that involves human interaction during every dispersion measurement. The principal human role is to choose the frequency band of measurement and to guide the extraction of the fundamental mode from noise, scattered and multipathed signals, overtones, and fundamental modes of different wave type. Continental regions at high southern latitudes are sampled mostly by surface waves that emanate from mid-ocean ridge earthquakes. The major obstacle in obtaining reliable broadband measurements therefore is the strong refraction that intermediate- and short-period surface waves suffer at the continental margins. Strongly excited Rayleigh waves, for example, are commonly observed on transverse components. In addition, Love wave overtones can interfere in the measurement of short-period fundamental Love waves. Discretion and insight must be exercised to obtain reliable Love wave measurements. As a consequence, human interaction in making measurements is particularly necessary below 40–50 s period in the Southern Hemisphere.

We use group velocity measurements from 18 to 175 s period for Rayleigh waves and from 20 to 150 s period for Love waves. The phase velocity measurements were performed at Harvard University and Utrecht University separately, and we merge these data sets into a single data set. The phase velocity measurements extend from 40 to 150 s for both Rayleigh and Love waves. These data sets are described by *Ekstrom et al.* [1997] and *Trampert and Woodhouse* [1995]. We choose phase velocity measurements only from earthquakes shallower than 50 km, which reduces the Utrecht data set appreciably. We use similarly shallow earthquakes for the group velocity measurements which simplifies the interpretation of the measurements and reduces the size of the source group time shifts, which we do not attempt to correct [*Levshin et al.*, 1999].

We measured the group velocities following earthquakes that occurred from 1977 to 1998 at stations from the Global Digital Seismograph Network (GDSN), Global Seismic Network (GSN), Geoscope, and SKIPPY networks. The phase velocity data are from 1980–1995 and 1989–1995 for the Utrecht and Harvard data sets, respectively.

At each period and wave type we identify and cluster measurements that follow similar paths, compute cluster RMS, and reject outliers. The cluster analysis has been previously described, for example, by RL1998. The cluster RMS is shown in Figure 3, where we report the results for the measurements obtained at Harvard University and Utrecht University separately. We identify the aggregated cluster RMS, prior to outlier rejection, with the average measurement error. The Harvard researchers performed their own clustering and data rejection, which probably explains why the Harvard data have a lower cluster RMS that the Utrecht data. The cluster RMS for the Utrecht data may therefore provide a better estimate of measurement error for phase velocities. The cross consistency between the Utrecht and Harvard data sets is about the same as the internal consistency of the Utrecht data set. Typical measurement errors are 20–25 m/s for group velocities, except at very short periods, and 10–15 m/s for phase velocities, except for long-period Love waves. Because, as Figure 4 shows, the amplitudes of the partial derivatives for group velocities [*Rodi et al.*, 1975] are about twice as large as for phase velocities, the amplitudes of the group velocity signals are about twice as large as the phase velocity signals. The group velocity and phase velocity signal-to-noise ratio therefore is about the same if the noise is considered to be measurement error.

Before merging the Harvard and Utrecht phase velocity measurements, we follow the outlier rejection by combining the remaining measurements within each cluster into a single measurement for the cluster. We do this separately for the Harvard and Utrecht data sets. This reduces the size of each data set considerably. We then merge the two individually declustered data sets and perform the cluster analysis again on the merged data set. Because each data set has been declustered individually, clusters within the merged data set usually contain only two measurements, one from the Harvard data set and one from the Utrecht data set. These measurements are averaged if they agree within a

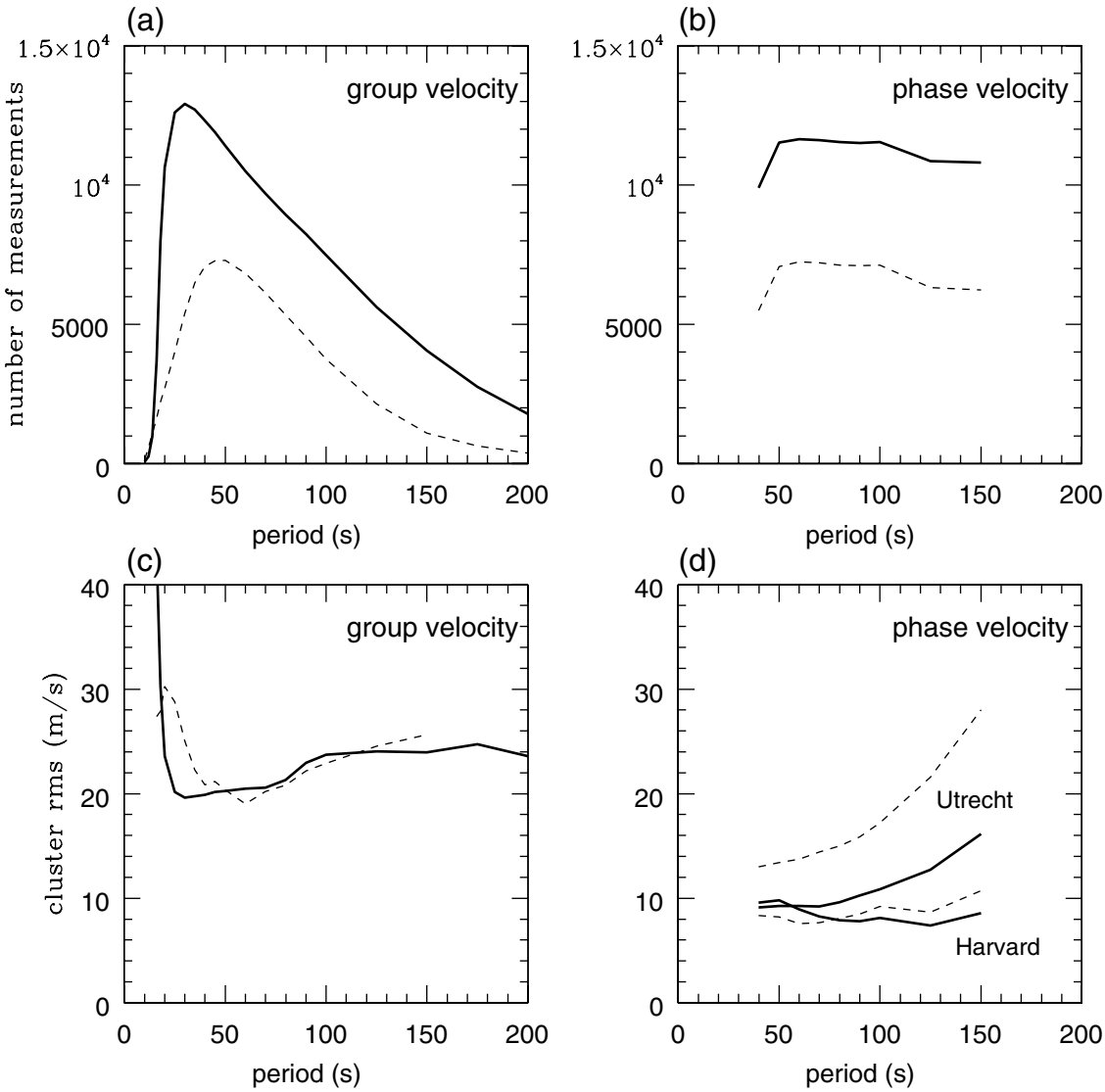

Figure 3. Statistical summary of the group and phase velocity measurements. (a, b) Number of measurements used in the surface wave tomography. (c, d) RMS variation of all measurements that occur within clusters with similar ray paths. The University of Colorado's group velocity measurements are given in Figures 3a and 3c; the combined phase velocity data set from Harvard University and Utrecht University is given in Figures 3b and 3d. Solid lines are the Rayleigh wave results, and the dashed lines are the Love wave results. The number of measurements is for wave paths in the Southern Hemisphere (some part of the ray extending below 20°S), but the cluster RMS is a summary of the global data.

specified tolerance, and both are discarded if they disagree. We do not decluster the group velocity data set, but we do perform the cluster analysis in order to reject outliers. The total number of measurements in the Southern Hemisphere (some part of the ray extending below 20°S) is shown in Figure 3. Because the group velocity data set involves human interaction to choose the frequency band of measurement for each source:station pair, the number of group velocity measurements depends on frequency and wave type. The number of phase velocity measurements is only weakly dependent on frequency.

Examples of data density are plotted in Figures 5 and 6. Globally, coverage is better for Rayleigh waves than Love waves, but this is particularly true in the Southern Hemisphere. This is presumably caused by attenuation and scattering because path lengths are on average longer in the Southern than in the Northern Hemisphere. Homogeneous coverage at long periods is also difficult to achieve in the Southern Hemisphere. This is because most of the seismicity surrounding Antarctica occurs at mid-ocean ridges and ridge events tend to be smaller in magnitude than events in subduction zones. Consequently, although there are fewer Love wave group velocity measurements than Love wave phase velocity measurements at long periods, path coverage across Antarctica is at least as good for the group velocities. Most of the phase velocity paths are concentrated east of Australia and across the southern Pacific.

3. Method of Inversion

The inversion for a shear velocity model breaks into two principal steps: (1) surface wave tomography and (2) inversion for a shear velocity model. The starting point for both steps is an

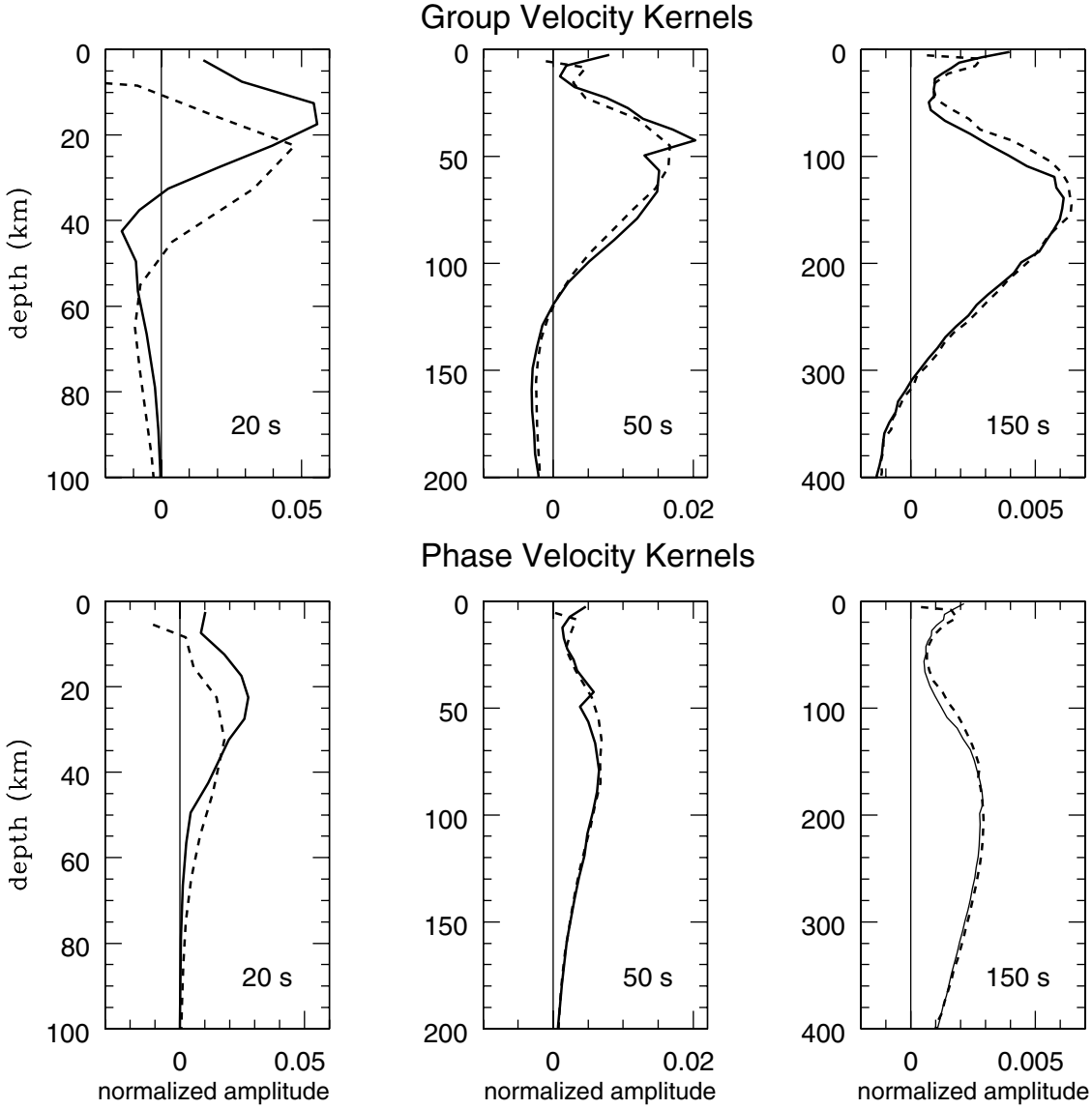

Figure 4. Rayleigh wave partial derivatives, or sensitivity kernels, of (top) group and (bottom) phase velocity with respect to isotropic shear velocity as a function of depth at the periods indicated. Solid lines are for a typical continental Craton, and dashed lines are for a typical ocean basin. Amplitudes are normalized by the maximum amplitude of the group velocity partial derivative in each column. Group velocity kernels are more than twice the amplitude of phase velocity kernels at each period and peak nearer to the surface. Phase velocities are sensitive to greater depths at each period because of the sign change in the group velocity kernels. Ocean-continent differences in the kernels are only significant near the short-period end of the studied frequency band.

initial model comprising CRUST5.1 [*Mooney et al.*, 1998] in the crust and isotropic S20A [*Ekstrom and Dziewonski*, 1998] in the mantle. We modify S20A in two ways. First, we introduce radial anisotropy equal to that in PREM. Second, we take the lateral variations in S20A with respect to the 1-D model ak135 [*Kennett et al.*, 1995] rather than PREM [*Dziewonski and Anderson*, 1981] which eliminates the discontinuity at 220 km that exists in PREM.

3.1. Step 1: Surface Wave Tomography

Surface wave tomography is the inference of maps of surface wave velocities for each wave type (Rayleigh, Love) and period. We use the method of BRL2001 to construct maps on a $2^\circ \times 2^\circ$ nodal grid worldwide subject to the following objective function for an isotropic model $\mathbf{m}$ consisting of velocity perturbations relative to the initial model:

$$(\mathbf{Gm} - \mathbf{d})^T \mathbf{C}^{-1} (\mathbf{Gm} - \mathbf{d}) + \alpha^2 ||F(\mathbf{m})||^2 + \beta^2 ||H(\mathbf{m})||^2. \quad (1)$$

Equation (1) is a linear combination of data misfit, model roughness, and amplitude of the perturbation to the initial model. $\mathbf{G}$ is the forward operator that computes the surface wave group or phase travel time from a model [*Woodhouse*, 1988], $\mathbf{d}$ is the data vector whose components are the observed travel time residuals relative to the initial model, $\mathbf{C}$ is the data covariance matrix or matrix of data weights, F is a Gaussian spatial smoothing operator, and H is an operator that penalizes the norm of the model in regions of poor path coverage. The method is described in detail by BRL2001. We note here that the spatial smoothing operator is

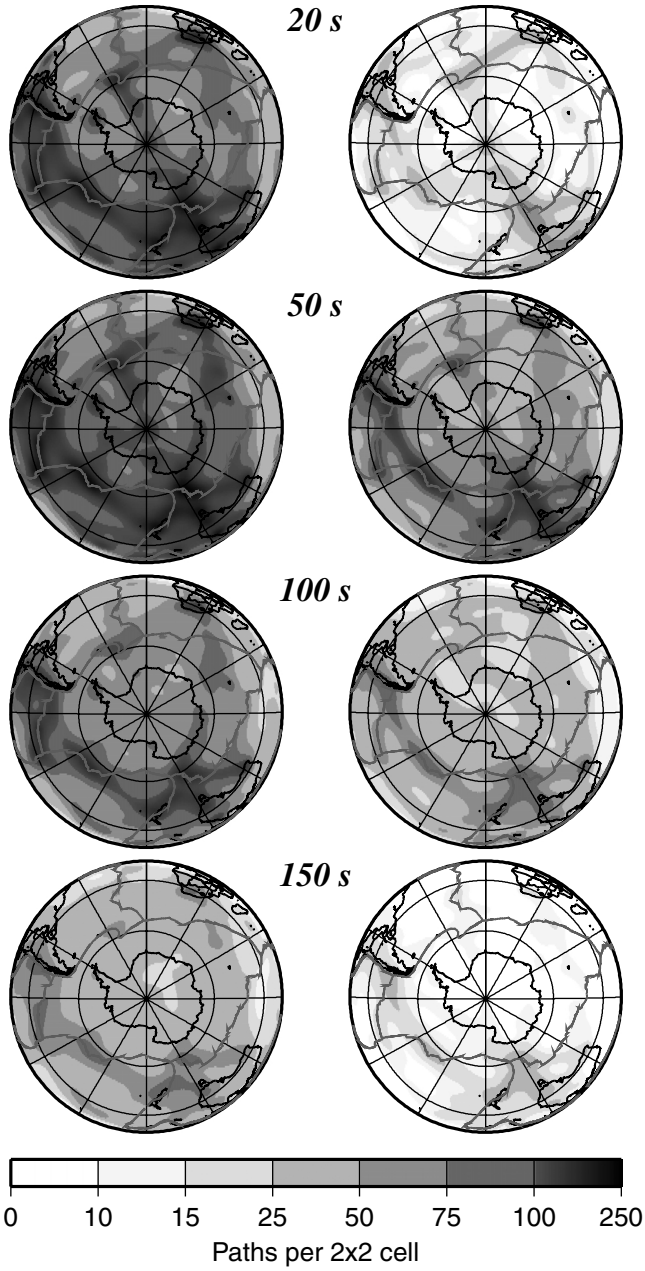

Figure 5. Path density of the data used in the group velocity tomography. Path density is defined as the number of measurements that intersects each 2° × 2° cell (∼50,000 km^2). Path coverage is better for Rayleigh waves than for Love waves and tapers off at short and long periods.

defined over a 2-D tomographic map as

$$F(\mathbf{m}) = \mathbf{m}(\mathbf{r}) - \int_S S(\mathbf{r}, \mathbf{r}')\mathbf{m}(\mathbf{r}')d\mathbf{r}', \tag{2}$$

where S is a smoothing kernel:

$$S(\mathbf{r}, \mathbf{r}') = K_0 \exp\left(-\frac{|\mathbf{r} - \mathbf{r}'|^2}{2\sigma^2}\right), \tag{3}$$

$$\int_S S(\mathbf{r}, \mathbf{r}')d\mathbf{r}' = 1, \tag{4}$$

and σ is the spatial smoothing width or correlation length. The strength of the model norm penalty depends on path density. The dispersion maps revert to those computed from the initial model in regions of poor path coverage (<∼20 paths per 2° × 2° cell).

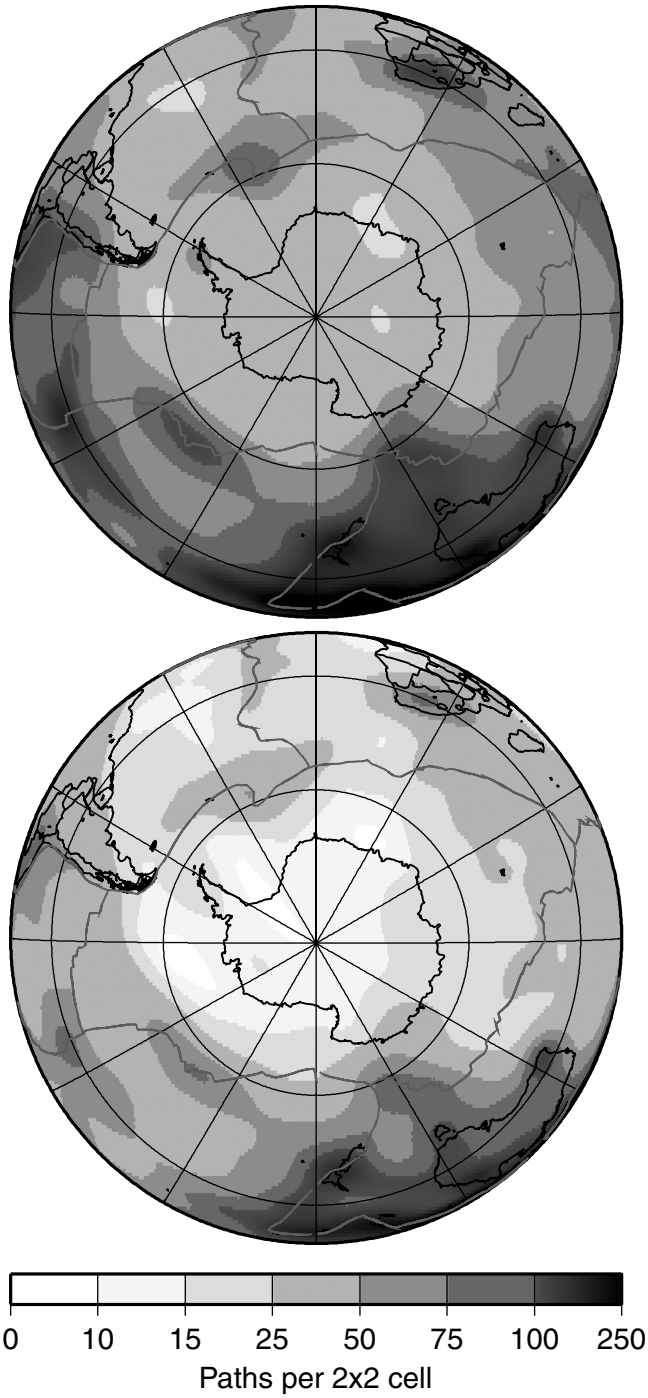

Figure 6. Path density, as defined in Figure 5, for the phase velocity data with the 100-s Rayleigh wave at top and the 100-s Love waves at bottom. Path density for phase velocity is roughly independent of period, so other periods are similar.

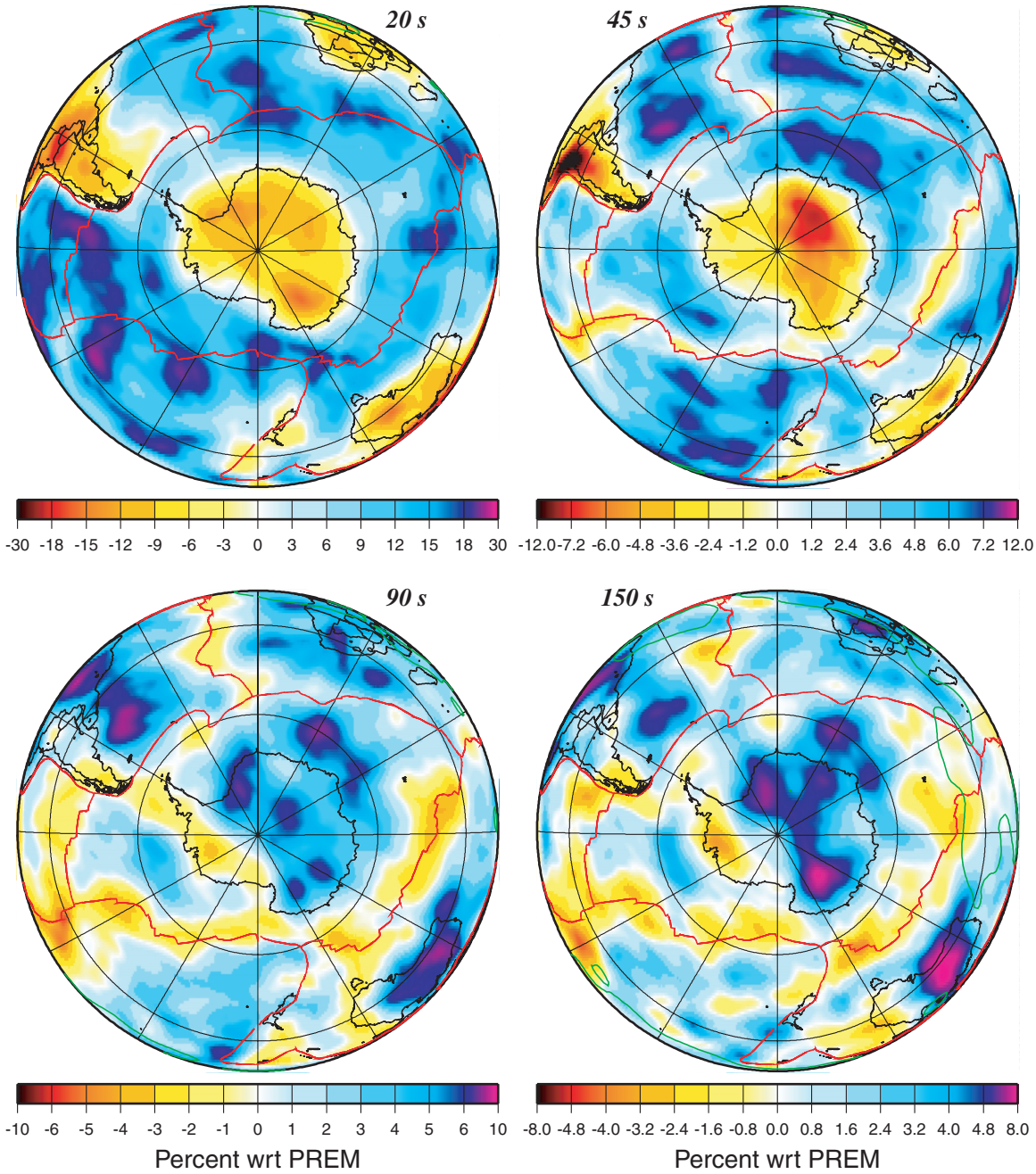

Plate 1. Estimated surface wave group velocity maps at a variety of indicated periods for Rayleigh waves. The green lines shown here and in Plates 2 and 3 are contours of 20 paths per 2° × 2° cell and therefore demarcate the regions poorly covered by the data. Their absence from a map means that path density is everywhere greater than 20 paths per 2° × 2° cell.

Values at spatial points between nodes are computed with bilinear interpolation.

Damping and regularization are discussed in detail by BRL2001. The choice of the damping coefficients α and β and the smoothing width σ is ad hoc. In particular, we produce a set of maps with variable damping for each wave type and period, and then we choose damping parameters that produce relatively smooth features with few artifacts such as streaking or spotting. We find that a spatial smoothing width σ of 250 or 300 km is appropriate. RL1998 provides an example using a different tomographic method, but the idea is the same. The smoothness constraint α is chosen to be constant over a broad frequency band, but we generally strengthen it at long periods because the maps tend to be more prone to artifacts and the Fresnel zone of the wave broadens.

We estimate tomographic maps in the following period bands: Rayleigh group velocity, 18–175 s; Love group velocity, 20–150 s; and Rayleigh and Love phase velocity, 40–150 s. We show examples of estimated dispersion maps in Plates 1–3. The contours of 20 paths for each 2° × 2° cell are marked in these figures to identify the poorly covered regions.

The ability of the tomographic maps to fit the raw measurements is shown in Figure 7 and is compared with the fit

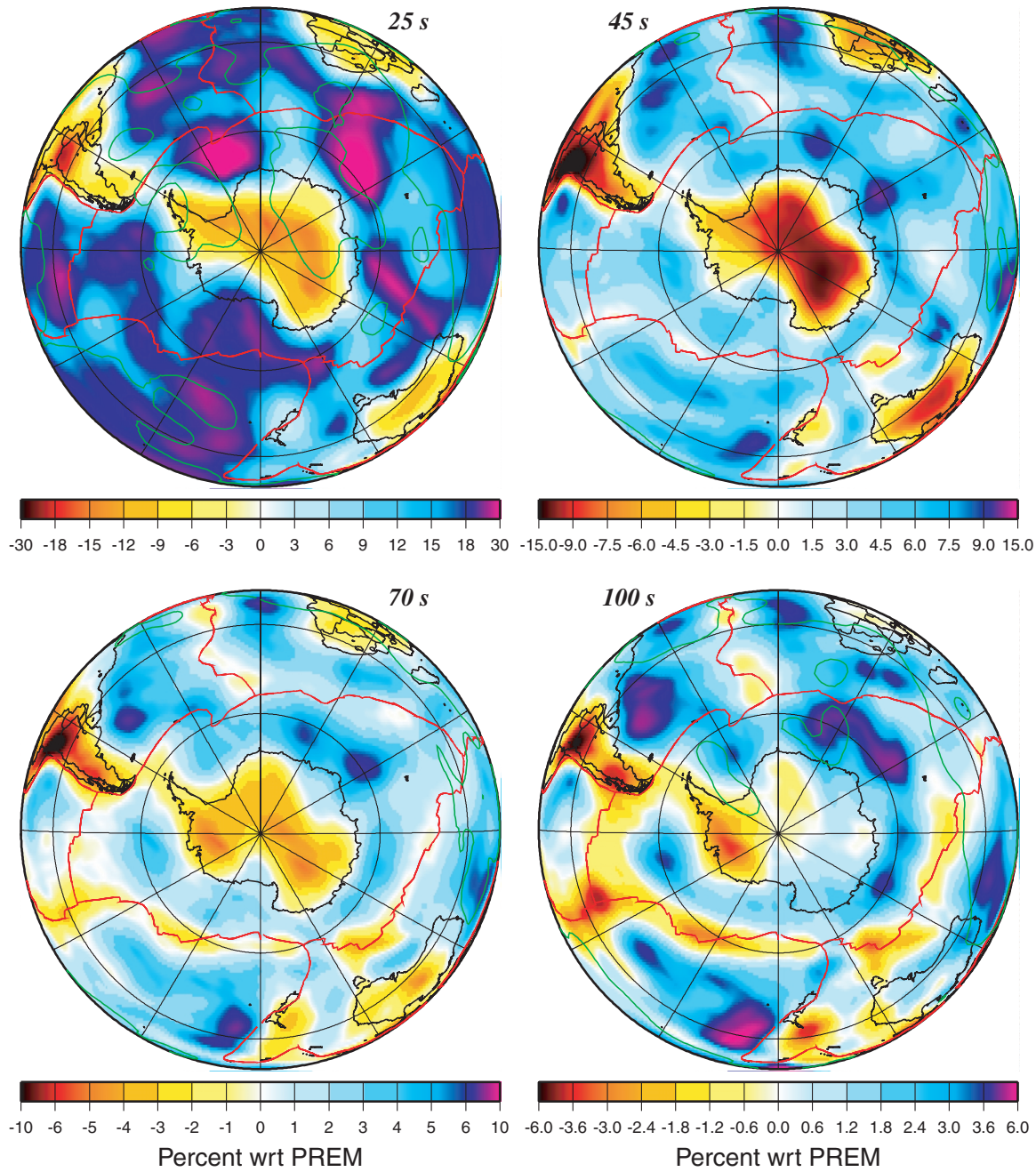

Plate 2. Estimated surface wave group velocity maps at a variety of indicated periods for Love waves. The green lines are described in the caption of Plate 1.

produced by a globally averaged model and the initial model. Group velocity measurements typically are fit by the estimated tomographic maps to between 40 and 50 m/s and phase velocity data to 20 and 40 m/s. If the cluster RMS in Figure 3 is interpreted as measurement error, comparison between Figures 3 and 7 reveals that RMS misfit with our estimated tomographic maps is about twice the measurement error except at short periods. This is true both for group and phase velocities. Below ~25 s for Rayleigh waves and ~35 s for Love waves, group velocity misfit increases to well above twice the measurement error. There are three reasons for this. The first two reasons are related to the fact that at shorter periods the waves become more sensitive to crustal structures. (1) Crustal structures require smaller-scale features to model accurately than those that appear in the inversion. (2) They also produce systematic bias caused by unmodeled wave propagation effects, such as off-great-circle propagation. The third reason, however, is the most important. (3) Path coverage degrades rapidly for short periods because path lengths are, on average, longer in the Southern Hemisphere than in the Northern Hemisphere. Our tomographic method reverts to the initial model in regions of poor path coverage, and the initial model does not fit the data well at short periods.

It is common practice in tomographic studies to report resolution. The results of resolution analyses should be greeted with a skepticism because they ignore both random and systematic measurement errors. For the sake of completeness, however, we will briefly present the results of a resolution analysis. We

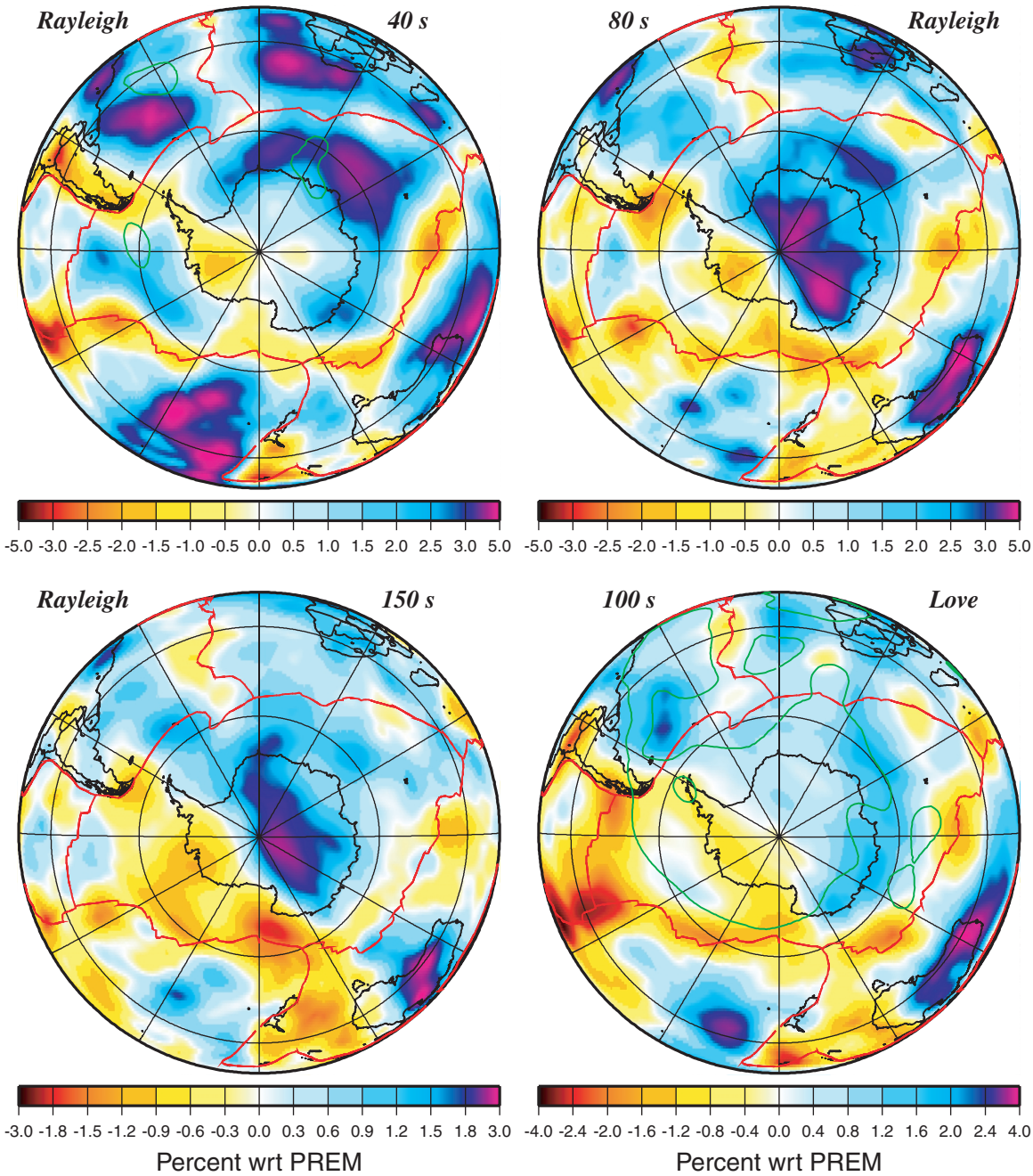

Plate 3. Estimated surface wave phase velocity maps at a variety of indicated periods and wave types. The green lines are described in the caption of Plate 1.

use the method of BRL2001, which constructs the classical resolution matrix at every node of each dispersion map. This method may be improved by using the Fresnel Zone [e.g., *Dahlen and Tromp*, 1998] to define the sensitivity of each ray. Gaussian smoothing in model space defined by equations (3) and (4), however, is similar to the use of Gaussian beams in physical space. In essence, then, the method of BRL2001 uses "fat rays." We believe that the fact that these rays are not as wide as the Fresnel Zone at the middle of the ray is offset by the fact that unlike Fresnel Zones, the Gaussian beams do not taper near source and receiver and we use a very conservative method to summarize the resolution map. We summarize each resolution map by using the full width of the base of the cone that best fits the resolution map near its peak, which is much more conservative that the use of the standard deviation or other common estimates.

Figure 8 displays the estimates of lateral resolution for the tomographic maps using the method of BRL2001 which constructs the classical resolution matrix at every node of each dispersion map. At each node, therefore, there is a global map that displays how a delta-like velocity anomaly would be smeared and spread by the data distribution and damping applied in the inversion. Because of the bilinear interpolation between nodal points a delta-like function would appear as a cone with a specified nonzero value at the target node tapering linearly to zero at the adjacent nodes. To summarize the large volume of information in the collection of resolution maps, BRL2001 estimate a best fitting cone to the resolution map in the neighbor-

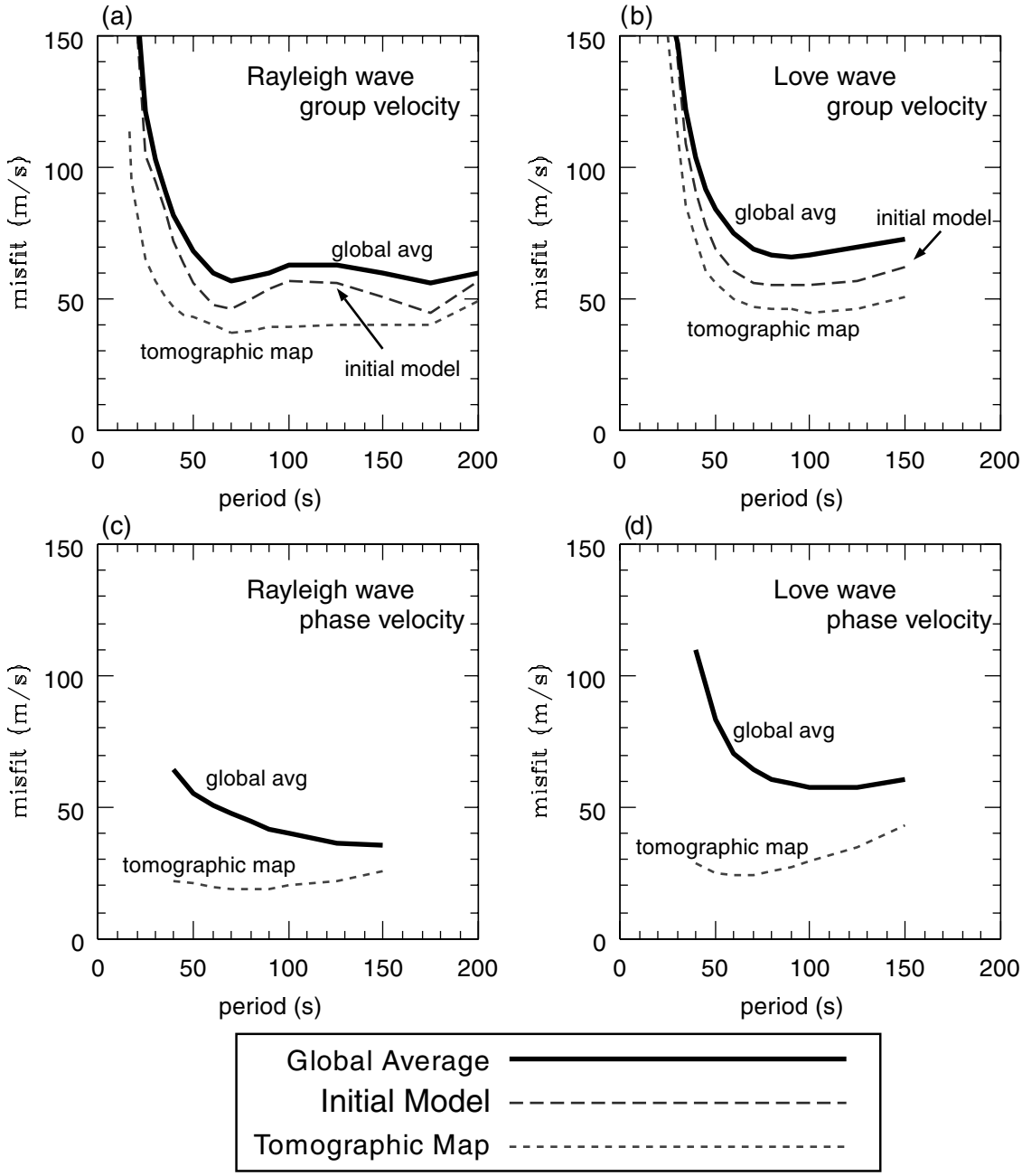

Figure 7. RMS misfit to the observed dispersion curves for three different sets of dispersion maps: the global average (solid lines), the initial model CRUST5.1/S20A (dashed lines), and the estimated tomographic maps (dotted lines) such as those shown in Plates 1–3. (left) Rayleigh waves and (right) Love waves, (top) group Velocity, and (bottom) phase velocity.

hood of the target node. They then equate the resolution at each target node with the width of the base of the best fitting cone. Optimal achievable resolution, therefore, is twice the node spacing, or 444 km with a $2^\circ \times 2^\circ$ grid.

Figures 8a and 8b show resolution maps for the 50 and 150 s Rayleigh wave group velocities. To a good approximation, the distribution of resolution follows path density as seen in Figure 5. With this conservative resolution scheme, full resolution of ~450 km requires about 100 paths per $2^\circ \times 2^\circ$ cell, which is rare at high southern latitudes. The average resolution south of 45° S for the 50 and 150 s Rayleigh wave group velocities is ~550 km and 720 km, respectively. Average resolution is summarized for all of the dispersion maps in Figure 8c, running ~600 km for Rayleigh waves and ~700 km for Love waves. Average resolution of uppermost mantle structures at high southern latitudes therefore is ~650 km but is better in certain locations.

For step 2 of the inversion we would like estimates of the uncertainties in the dispersion maps at every spatial point. The uncertainties, however, are not only difficult to estimate, their definition depends on a choice of length scale, which is largely arbitrary. For example, uncertainties would be very small if the maps were averaged over large areas but would increase dramatically as the averaging region approaches the grid spacing. For

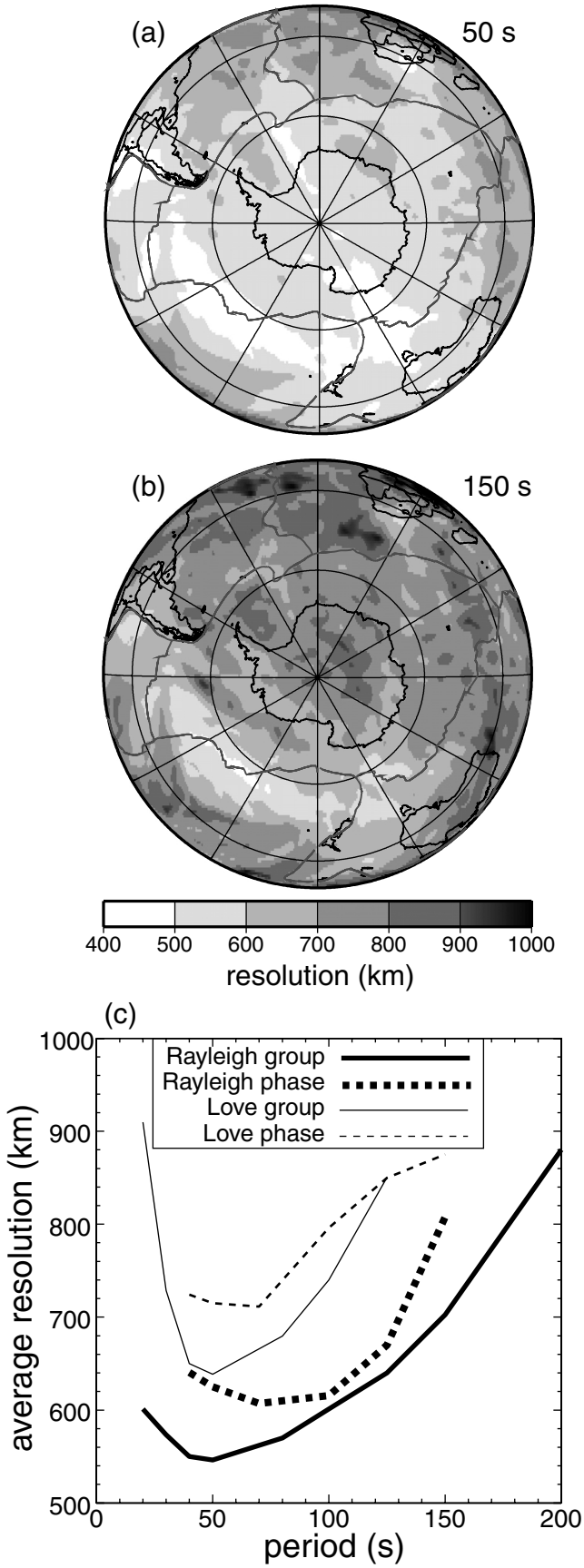

Figure 8. (opposite) Resolution analysis for the tomographic maps. (a) Estimated resolution map for the 50-s Rayleigh wave group velocity. (b) Estimated resolution map for the 150-s Rayleigh wave group velocity. (c) Average resolution south of 45°S latitude.

Table 1. A Priori Constraints on Allowed Models

Feature	Allowed Range	Reference
Crustal thickness	±5 km	CRUST5.1
Crustal S	±300 m/s	simple reference model
Upper and middle crustal P	±200 m/s	CRUST5.1
Lower crustal P	±300 m/s	CRUST5.1
v_{sh} and v_{sv} in uppermost mantle	±250 m/s	simple reference model
Bottom of zone of radial anisotropy	±30 km	220 km
Mantle isotropic S velocity	unconstrained	-
Mantle isotropic P	$d \ln v_p / d \ln v_s = 0.5$	ak135

this reason, we do not attempt to estimate spatially variable uncertainties. Instead, we use the average misfit of the tomographic maps to the dispersion measurements, shown in Figure 7, to represent the uncertainties in the dispersion curves everywhere. The advantage of using the a posteriori misfit as uncertainties is that it includes both theoretical errors (e.g., geometrical optics) and measurement errors and the shapes of the misfit curves probably are reasonable estimates of the uncertainties in the maps. The shortcomings include the fact that the misfit curves are not spatially variable and the absolute level of uncertainty is probably overestimated. Thus the misfit curves probably provide reasonable relative errors that overestimate the uncertainties in the tomographic maps.

3.2. Step 2: Shear Velocity Inversion

We use the method described by SR2001 to estimate the shear velocity model on a 2° × 2° grid globally, and we briefly describe the method here. The ultimate goal is to estimate the range of models that fit the dispersion maps subject to the uncertainties discussed in section 3.1 and a priori information. A priori information is introduced in two forms: implicit and explicit constraints. Implicit constraints are introduced through the choice of parameterization and explicit constraints are in the form of tolerances applied to the allowed perturbations to the starting model. Table 1 defines these tolerances. Crustal structures are fairly tightly constrained, particularly in v_p, but the strengths of both the isotropic and anisotropic perturbations in the mantle are largely unconstrained. The method is divided into three substeps, which are schematically outlined in Table 2. Each substep depends on an input model because the inversion is nonlinear.

Substep 1 is an iterative linearized inversion with a simple parameterization of the crust and upper mantle to a depth of 400 km. The method and parameterization are essentially the same as that described by *Villaseñor et al.* [2001] in the inversion for a shear velocity model beneath central Asia. The method is iterative because the sensitivity kernels change as the shear velocities in the crust and upper mantle change, particularly below ~30 s period (see example in Figure 4). The starting model is the same as that used in step 1 (CRUST5.1/S20A). In this substep the model is represented with six variables, including a shift in average crustal shear velocity, a perturbation in Moho depth, constant isotropic perturbations in mantle shear velocity in two layers (Moho to 220 km and 220–400 km), and the introduction of radial anisotropy slopes in both *SH* and *SV* velocities (v_{sh}, v_{sv}) between Moho and 220 km. This simple parameterization is best for continental regions and does not allow the data to be fit sufficiently well

Table 2. Outline of the Shear Velocity Inversion

Substep	Input Model	Method	Output Model(s)
Substep 1	initial model (CRUST5.1/S20A)	linearized inversion	simple reference model
Substep 2	simple reference model	simulated annealing	best fit model
Substep 3	best fit model	Monte Carlo	ensemble of acceptable models

everywhere. In addition, the method produces a single model rather than a range of acceptable models. We call the model that emerges from the linearized inversion the "simple reference model" and use it as the input model in substep 2.

Substeps 2 and 3 involve generalizing the model parameterization and resampling the enlarged model space near the simple reference model using a Monte Carlo method in order to constrain the range of models that fit the data. The generalized parameterization, consisting of 14 variables, is depicted in Figure 9. The key differences relative to the simple parameterization in substep 1 are the use of B splines in the mantle, the use of six crustal velocity perturbations (three each in v_s and v_p), and the introduction of a variable thickness to the radially anisotropic zone of the uppermost mantle. The model is highly overparameterized because we wish to consider a wider range of models that will fit the data than could be estimated unambiguously. Consistent with this, two of the B splines extend well below 400 km, although we consider the model to be only defined to 400 km. Linearized inversion with 14 model parameters is poorly posed, so we use simulated annealing to estimate a "best fit model" with the generalized parameterization [e.g., *Kirkpatrik et al.*, 1983; *Ingber*, 1989]. The objective function that the simulated annealing attempts to minimize is simply weighted ℓ_1 misfit:

$$\sum_i \sigma_i^{-1}[U_{\mathrm{obs}}(\omega_i) - U_{\mathrm{pred}}(\omega_i)] + \sum_j \sigma_j^{-1}[c_{\mathrm{obs}}(\omega_j) - c_{\mathrm{pred}}(\omega_j)], \quad (5)$$

where U and c are group and phase velocity evaluated on a discrete grid of frequencies ω for both Rayleigh and Love waves and σ_i and σ_j are the average group velocity and phase velocity RMS misfit provided by the tomographic maps, as shown in Figure 7. The notations "obs" and "pred" refer to observed and predicted velocities. In all three substeps, data are additionally downweighted if path density is low and/or a datum cannot be fit well. Lateral smoothing constraints arise only from the smoothing applied during the surface wave tomography, and a vertically smooth model is ensured by the use of the B splines.

We allow v_p to change both in the crust and mantle, although it is only an explicit variable in the crust, but we fix ρ and Q at the values in the initial model. Because surface wave data are nearly insensitive to v_p in the mantle, we compute v_p from the average of v_{sh} and v_{sv} by using the logarithmic scaling relation $d \ln v_s / d \ln v_p = 2.0$, where perturbations are taken relative to the 1-D model ak135. We compute density using the scaling relation $d \ln \rho / d \ln v_s = 0.4$ with respect to v_s in CRUST5.1 and S20A and fix Q at the PREM values.

The best fit model that emerges from substep 2 together with the a priori constraints on allowable perturbations to the model parameters define the region of model space that we search in substep 3 with the Monte Carlo method. An example of the outcome at a point in East Antarctica is shown in Figure 10 together with information about how well the dispersion curves extracted from the tomographic maps are fit at this point. Therefore, at each spatial point we estimate an ensemble of acceptable models that defines a corridor for the shear velocities that are consistent with the data. Acceptability is defined, as in substep 2, by using weighted misfit given by equation (5). A model is considered acceptable if the weighted misfit is no worse than about 33% larger than the best fit model. The Monte Carlo sampling of model space is continued until 2000 acceptable models are found at each spatial point. This typically requires the construction of about 30,000 models. The simple reference model produces a misfit that is, on average, ~40% higher than the best fit model and is included in the ensemble of acceptable models only at about one-third of the spatial nodes.

In order to summarize the information in each ensemble at each spatial point we use the middle of the corridor at each depth defined by the full range of models together with the half

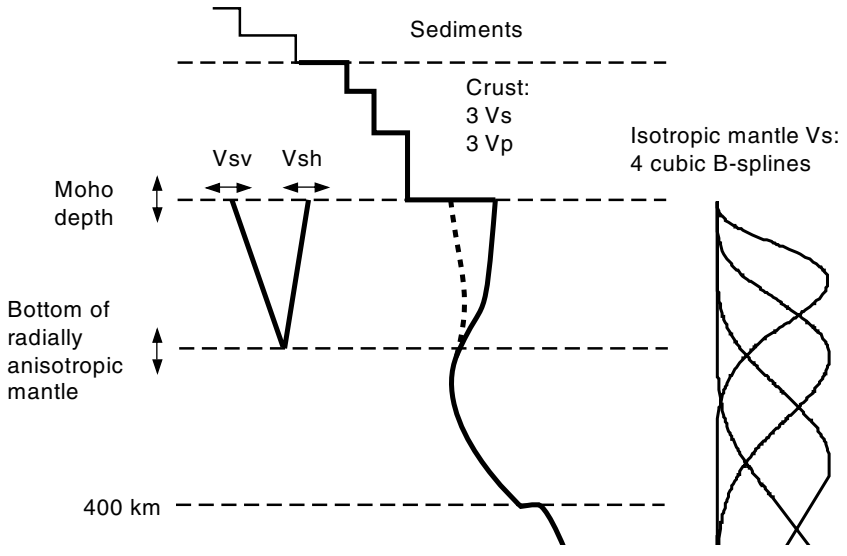

Figure 9. Parameterization of crustal and upper mantle structures used in substeps 2 (simulated annealing) and 3 (Monte Carlo resampling) of the shear velocity inversion. At each geographical point the parameterization includes 14 variables: a perturbation to sedimentary velocity, perturbations to both *S* and *P* velocities in each of three crustal layers, introduction of slopes in *SV* and *SH* velocities from Moho to a variable depth, and four cubic B splines in the mantle.

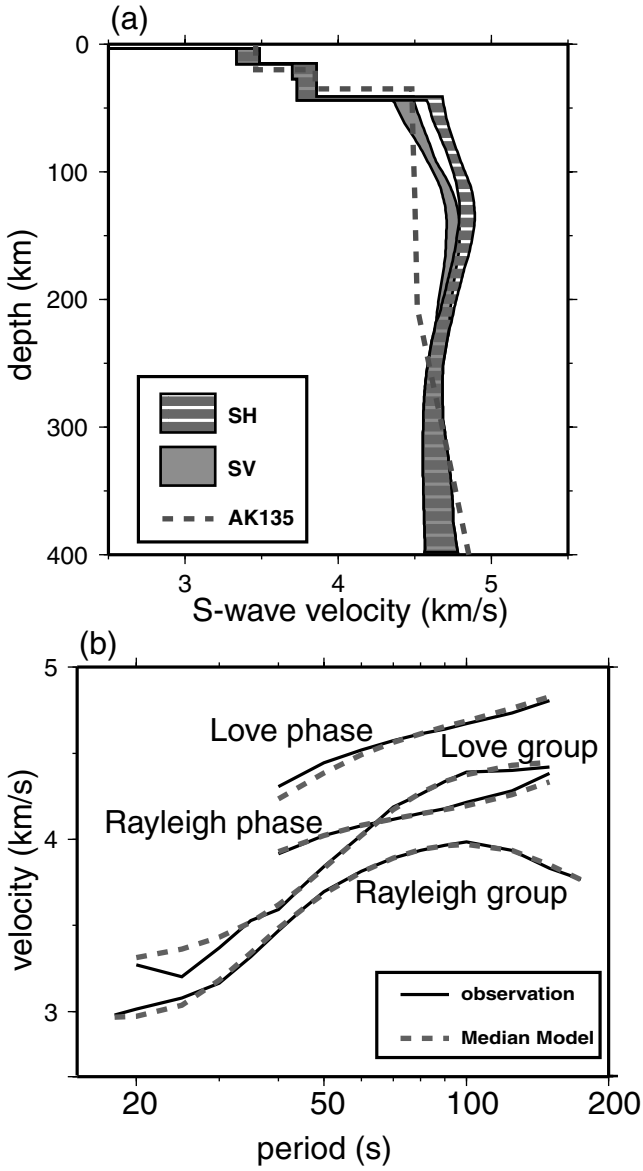

Figure 10. Results of the inversion for an ensemble of acceptable shear velocity models at a point in East Antarctica (80°S, 90°E). (a) Global model ak135 [*Kennett et al.*, 1995] plotted as the dashed line and the corridor that represents the full range of the ensemble of acceptable models at each depth. The bifurcation of the model in the uppermost mantle is due to radial anisotropy ($v_{sh} > v_{sv}$). (b) Fit to the Rayleigh and Love wave group and phase velocity curves provided by the median model. The observations, derived from the tomographic maps at this point, are plotted as solid lines, and the prediction from the median model is plotted as dashed lines.

width of the corridor. The half width of the corridor can be thought of as an uncertainty, but it is not a statistical estimate because the corridor is the full width of the acceptable models at each depth. It is probably a conservative estimate of uncertainty and is designed to encompass both random and systematic errors in the model. Because the middle of the corridor is usually indistinguishable from the median of the ensemble, we will refer to the model composed of the set of middle points as the "median model."

The use of the ensemble of acceptable models to quantify model uncertainty is not foolproof. After all, it simply summarizes the range of models, subject to a priori constraints, consistent with the tomographic maps. It is not impossible that systematic errors in the tomographic maps will bias the model without affecting the corridor of acceptable models. Another potential problem is that the resolution of the tomographic maps changes with period and wave type. It is also possible that this variable resolution could systematically bias the model in a way that is not reflected in the width of the ensemble's corridor. These caveats aside, we believe that at the vast majority of locations and the depths the ensemble of acceptable models effectively and accurately quantifies our confidence in the model.

If the half width of the corridor of acceptable models at a given depth is less than the difference between the median model and the 1-D ak135, then we say that the observed anomaly is "persistent" at that depth. This means that all of the acceptable models are either faster or slower than ak135 at this depth. If a feature of the median model is persistent, we consider it to be robust and worthy of interpretation. We will use this notion of persistence in discussing the median model below.

Although Monte Carlo and related inversion methods have a long history and are now common in surface wave seismology [e.g., *Levshin et al.*, 1966; *Keilis-Borok and Yanovskaya*, 1967; *Press*, 1968; *Calcagnile et al.*, 1982; *Lomax and Snieder*, 1994; *Shapiro et al.*, 1997], we are unaware of studies that have performed it on a global scale largely because of computational expense. Consequently, global-scale models typically lack uncertainty information. We consider about 30,000 models at each of the ~16,000 spatial nodes on which the model is defined globally. The forward problem for broadband group and phase velocities must therefore be solved on the order of 10^9 times to estimate the ensemble of acceptable models worldwide. On current generation workstations each forward prediction takes more than 10^{-1} s to perform using the best normal mode eigenfunction codes [e.g., *Woodhouse*, 1988]. Approaching the problem in this way would require more than 3 CPU years. *James and Ritzwoller* [1999] describe a third-order perturbation theoretic method that accelerates the forward problem by a factor of ~200 and allows the full ensemble of models to be characterized in ~1 CPU week running concurrently on several workstations. The perturbation method works best if the starting model is close to the estimated model. The purpose of substeps 1 and 2, then, is to speed the Monte Carlo sampling by providing a good enough starting model to guarantee the accuracy of the perturbation method in substep 3.

Figures 11–13 attempt to summarize the fit to the tomographic maps provided by the median model. Figures 11 and 12 are misfit maps in which the gray scales are chosen based on the misfit to the dispersion data provided by the tomographic maps, σ_i for group velocities and σ_j for phase velocities in equation (5). Over a fairly broad frequency range, σ_I is ~40 m/s, and σ_j is ~25 m/s. The shaded regions in Figures 11 and 12 therefore are areas in which the misfit is worse than ~2σ. Love waves are fit considerably worse than Rayleigh waves principally because Love wave path coverage is lower and they are weighted lower in the inversion. Additionally, the quality of the Love wave maps at high southern latitudes is simply worse than the Rayleigh wave maps, and the fit to them is not expected to be as good. As a consequence, v_{sh} is not as well known as v_{sv} in the upper mantle.

Misfit summary statistics appear in Figure 13 which compares the fit to the dispersion maps of the median model to that of the initial model (CRUST5.1/S20A). The dispersion maps are fit, on average, close to the measurement errors that appear in Figure 3. This is consistent with our belief that the uncertainties defined by the misfit of the tomographic maps to the data in Figure 7 are conservative. The pattern of misfit agrees with that in Figure 7,

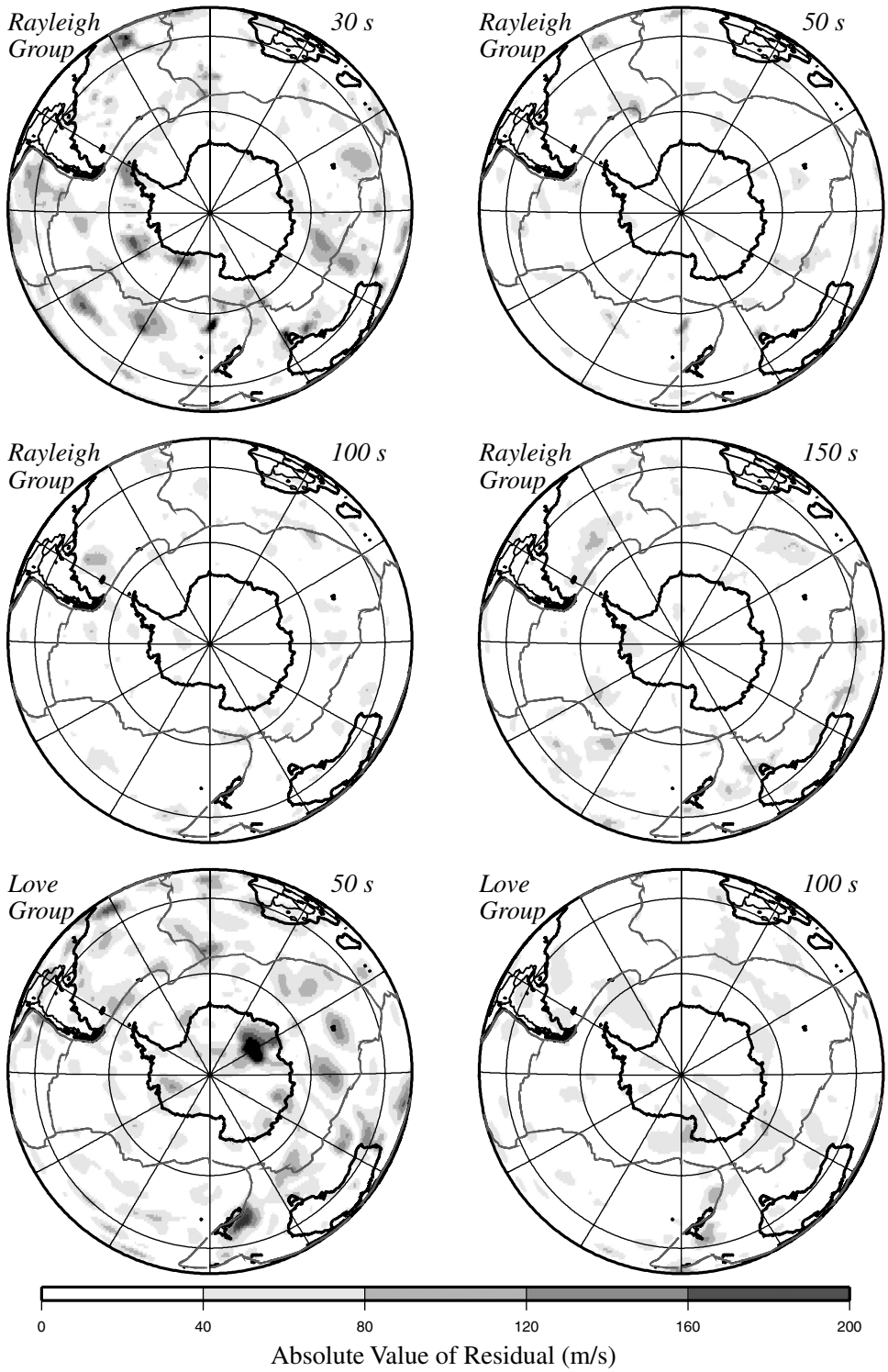

Figure 11. Spatial patterns of the absolute value of the residuals, defined as the difference between the observed dispersion maps and those predicted by the median model for selected group velocities. Units are m/s.

confirming that the values of σ_i and σ_j defined by Figure 7 provide good relative error estimates.

4. Discussion

We have estimated an ensemble of acceptable models that fit the dispersion curves extracted from the tomographic maps at each spatial point. Figure 10 presents one example and a few others appear in Figure 14. There are 2000 acceptable models constructed at every one of the ~16,000 spatial nodes worldwide. To summarize this large volume of information, we use the middle of the ensemble of acceptable models at each depth on each of the spatial nodes and refer to this as the median model. In addition, to summarize the variability of the ensemble, we use the half width of the full range of the velocities at each depth.

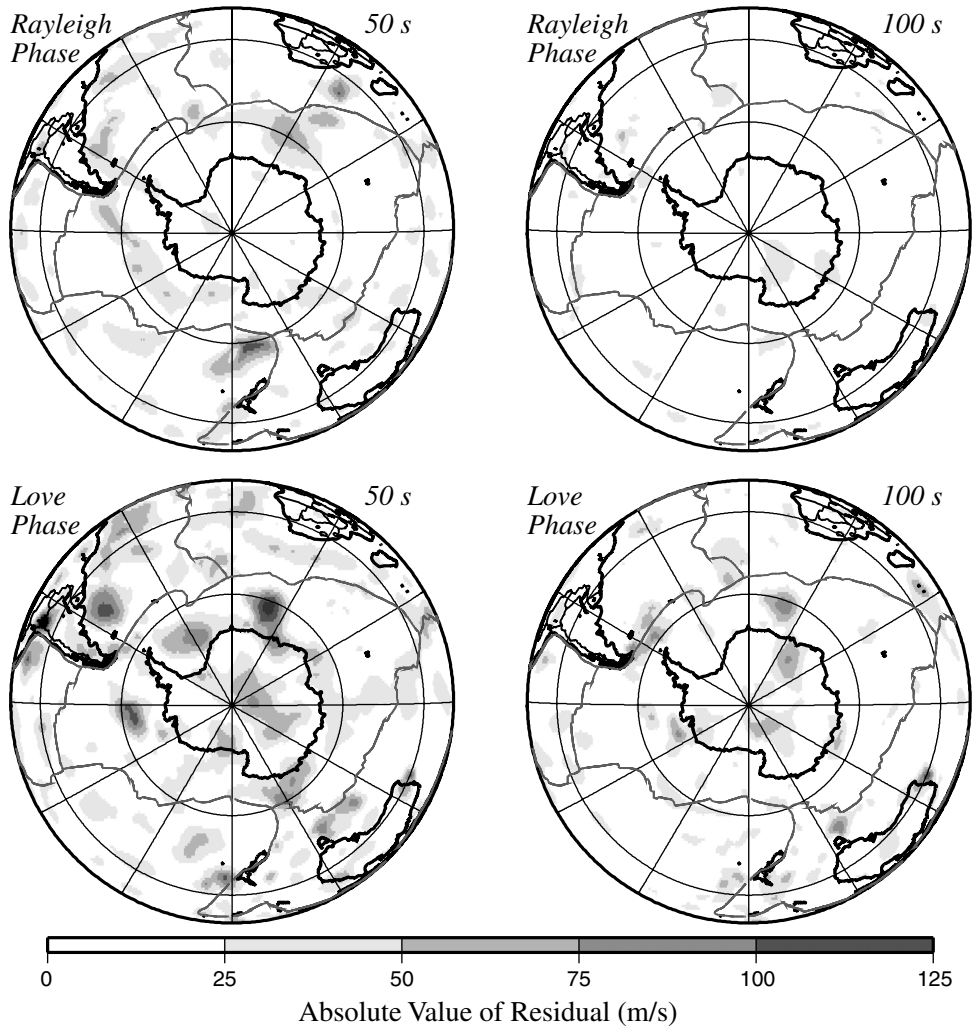

Figure 12. Spatial patterns of the absolute value of residuals, as defined in Figure 11, for selected phase velocities.

As Table 1 indicates, we have placed stronger constraints on allowed structures in the crust than in the mantle. That is, the resulting models remain closer to the initial crustal model (CRUST5.1) than they do to the initial mantle model (S20A). For this reason, the crustal model contains less information and is probably not as reliable as the mantle model. Moreover, CRUST5.1 is not as accurate in Antarctica as in other continents. For these reasons, we do not emphasize the crustal model here. However, we show crustal thickness from the median model in Figure 15. Crustal thickness averages ~27 km in West Antarctica, being slightly greater in Marie Byrd Land and beneath the Ellsworth Mountains and Pensacola Mountains, and substantially less in the Ross Embayment. Crustal thickness in East Antarctica averages ~40 km in the median model, with maximum Moho depths approaching 45 km.

The purpose of estimating ensembles of acceptable models is to identify the robust features of the model that are worthy of interpretation. We refer to velocity anomalies relative to ak135 that appear in every one of the acceptable models as the persistent features of the model. We identify persistent features by drawing a contour that encircles all velocity anomalies that appear in every one of the ensemble of acceptable models. For graphical simplicity these contours are absent from the horizontal slices of the median model found in Plate 4 but are included in the vertical slices of the model shown in Plate 5. We will note a few of the persistent features in the following discussion.

4.1. East Antarctic Craton

Most of East Antarctica is characterized by high-velocity anomalies on the long-period dispersion maps in Plates 1–3. This is particularly true for Rayleigh waves which sample deeper than Love waves (e.g., Figure 4). This feature is large enough to have been resolved as a high-velocity anomaly in previous studies, both regionally [e.g., *Roult et al.*, 1994] and at global scales [e.g., *Montagner and Tanimoto*, 1991; *Zhang and Tanimoto*, 1993; *Trampert and Woodhouse*, 1995; *Masters et al.*, 1996; *Ekstrom et al.*, 1997]. The amplitudes of the dispersion anomalies are not uniform over East Antarctica but are typically largest in Wilkes Land. As shown in Figure 10 and Plate 4, the uppermost mantle in East Antarctica is much faster than global averages such as ak135 down to a depth of 220–250 km depending on location. As Plate 5 demonstrates, the onset of the high-velocity anomalies in the uppermost mantle is very rapid across the Transantarctic Mountain front. There is no low-velocity zone underlying East Antarctica. Although the vertical velocity gradient changes sign in most of the ensemble of acceptable models between ~150 and 250 km (e.g., Figure 10), the shear velocities in this depth range remain

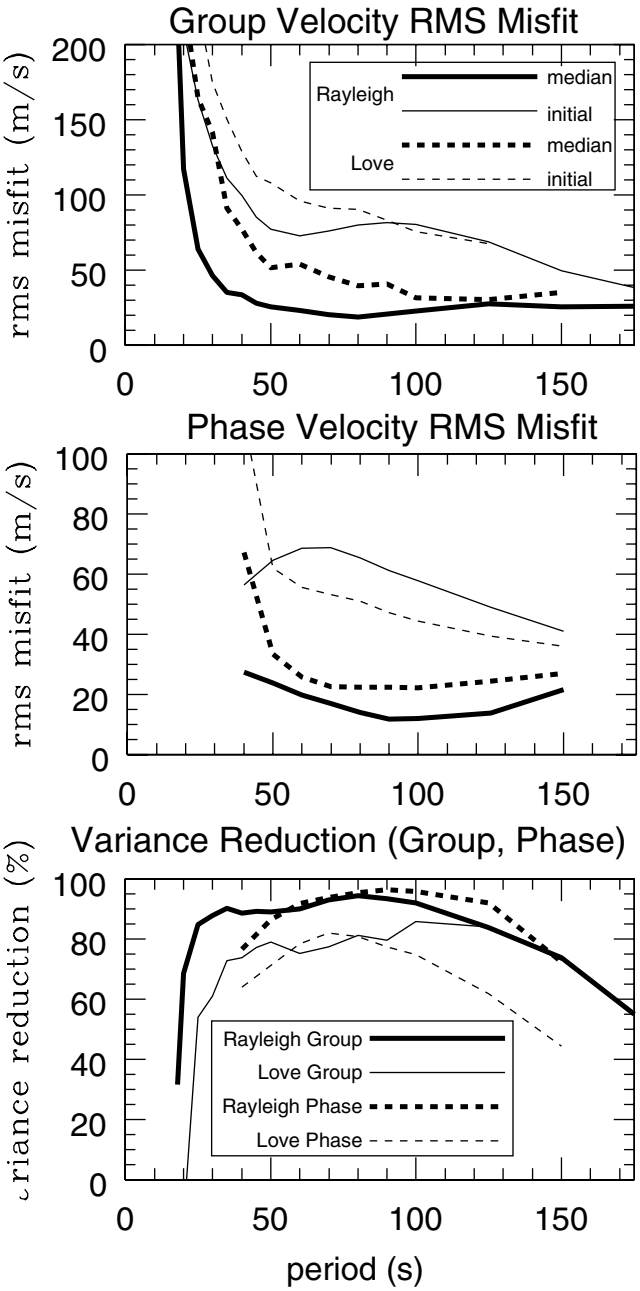

Figure 13. Summary of the fit between the observed dispersion maps and predictions from the median model. (top) Group velocities. RMS misfit is plotted for the initial model (CRUST5.1/S20A) and the median model according to the legend. (middle) Same as Figure 13 (top) but for phase velocities. (bottom) Variance reduction relating predictions from the median model to the initial model according to the legend.

above the global average. The magnitude of the uppermost mantle high-velocity anomaly and its depth extent are variable across East Antarctica, as they are across the other cratons around the globe. These variations may be due to compositional inhomogeneities or other variations in the manner in which the cratons formed. Alternately, they may be thermal in nature, perhaps being characteristic of convection in the sublithosphere [e.g., *Jaupart et al.*, 1998]. Topographic undulations on the underside of the cratons may therefore reveal the planform of small-scale convection (P. Molnar, personal communication, 2001).

Whether East Antarctica is a shield has been questioned by a number of researchers. For example, on the basis of Rayleigh and Love wave group velocity measurements from 15 to 70 s period for wave paths crossing East Antarctica, earlier studies [e.g., *Bentley*, 1973] argued that East Antarctica is not a classical shield but is more similar to a stable platform. Figure 16 confirms the observations that are the basis for these studies for a point in Wilkes Land, by showing that the short- and intermediate-period Rayleigh wave group velocities are, on average, slower than those from eight other cratonic regions. At longer periods and for phase velocities, however, the dispersion of surface waves in East Antarctica is more similar to the other cratons. In fact, Figure 2 suggests that the ice sheet is at least partially responsible for reducing the group velocities at short and intermediate periods in East Antarctica. The ensemble of acceptable models at the same point in Wilkes Land is shown in Figure 16c to be consistent with the upper mantle beneath the other eight cratonic regions both in the maximum amplitude and the depth extent of the high-velocity anomaly. At least in Wilkes Land, East Antarctica is a "typical shield." Variations in upper mantle velocities across East Antarctica and other cratonic regions may cause us to rethink what is meant by a "typical" shield, however.

4.2. West Antarctic Rift

In striking contrast with East Antarctica, much of West Antarctica is characterized by low-velocity anomalies on the long-period dispersion maps in Plates 1–3. These anomalies extend from the Ross Sea through the Ross Embayment, typically achieve their minimum values near the Byrd Subglacial Basin in Marie Byrd Land, and continue offshore west of the Antarctic Peninsula. They are therefore contiguous with the West Antarctic Rift System [e.g., *LeMasurier*, 1989; *Behrendt et al.*, 1991]. These features are distinguished from the high-velocity anomalies in East Antarctica and the Bellingshausen Sea both on the phase and group velocity maps for both Rayleigh and Love waves. Previous dispersion studies were able to provide a tantalizing hint of these anomalies, but it is probably fair to say that resolution was just out of reach.

We show a depth profile at a point beneath the Byrd Subglacial Basin in Figure 14a. Comparison with Figure 10a reveals a very different velocity structure in the upper mantle for West Antarctica than for East Antarctica. The crust is much thinner in the west, and there is a prominent asthenospheric anomaly in which velocities minimize at a depth of about 120 km. Normal mantle velocities are reestablished by ~200 km depth. The spatial distribution of the asthenosphere can be seen in Plate 4. By a depth of ~150 km the low-velocity anomaly under the West Antarctic Rift is indistinguishable from oceanic asthenosphere. This is clearly seen in Plate 5 (C-C′), which displays a vertical slice from near the East Pacific Rise, through the West Antarctic Rift, over the pole to the Kerguelen Plateau. The structure beneath the Byrd Subglacial Basin is distinct from normal oceanic lithosphere by its thicker crust and a less prominent lid overlying the asthenosphere.

The West Antarctic Rift may be one of the world's most poorly understood rift systems. It is believed to be what is left of a continuously propagating rift that started in the Jurassic when Africa separated from East Antarctica and proceeded clockwise to its present location in the Ross Embayment and West Antarctica. Volcanic activity has occurred at least since the early Cenozoic, and Holocene volcanism continues in the Ross Embayment [e.g., *Kiele et al.*, 1983], Marie Byrd Land [e.g., *LeMasurier*, 1989], and apparently under the ice sheet within the rift itself [e.g., *Blankenship et al.*, 1993; *Behrendt et al.*, 1994]. Extension is believed to have occurred in the Late Mesozoic and early Cenozoic [*Cooper et al.*, 1987; *DiVenere et al.*, 1994; *Luyendyk*

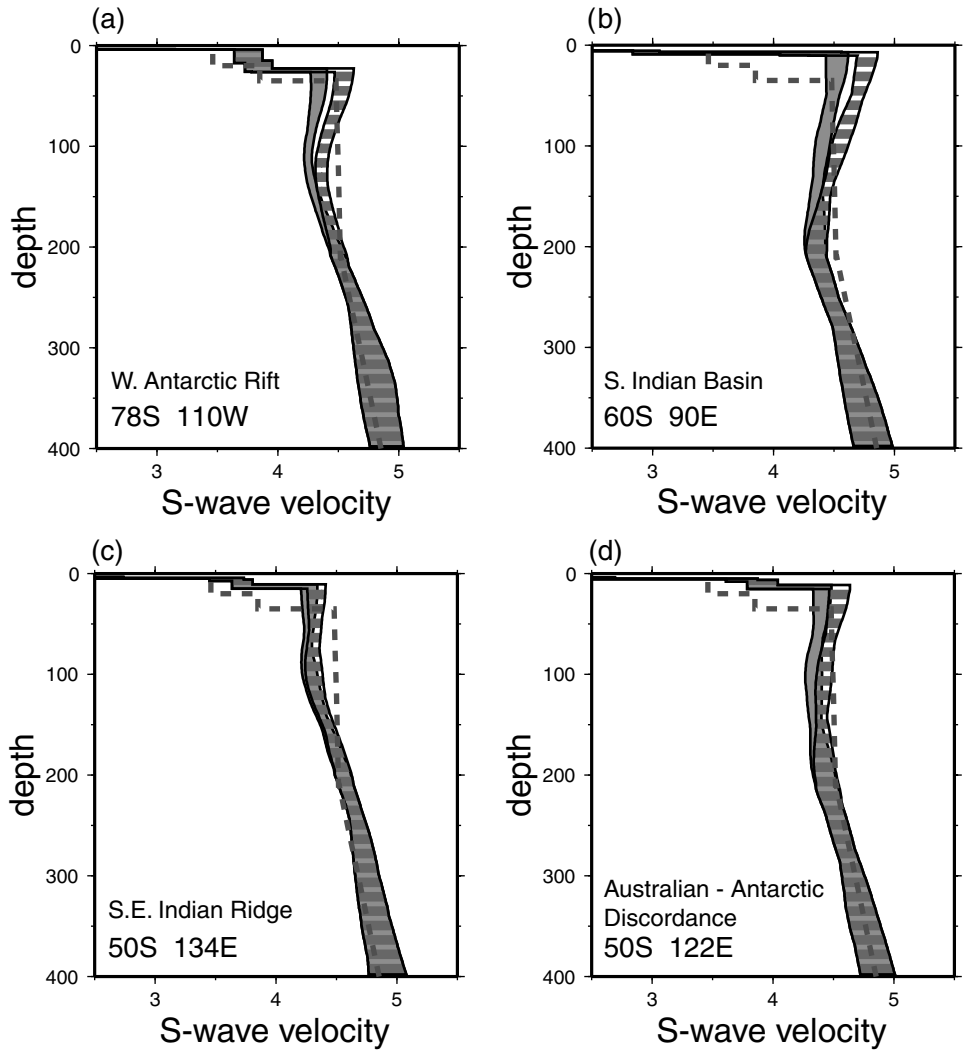

Figure 14. Ensembles of acceptable models at a number of geographical points, plotted as in Figure 10.

et al., 1996], and a recent paleomagnetic study points to an episode of mid-Cenozoic extension [*Cande et al.*, 2000], but the near absence of earthquakes in the West Antarctic Rift is often taken as evidence that the rift is not undergoing active extension today. A mantle plume under the rift has been proposed based on large volumes of subglacial and submarine volcanic rocks of late Cenozoic age [*Behrendt et al.*, 1992, 1994], and the inferred ocean island basalt chemistry of these rocks [*Hole and LeMasurier*, 1994]. *Behrendt et al.* [1996] recently supplemented this hypothesis to include lower lithospheric stretching [*Keen et al.*, 1994] to help account for the large area of late Cenozoic ocean island basalts.

Our model suggests that the upper mantle beneath the West Antarctic Rift is hot today, consistent with evidence of active volcanism underlying the West Antarctic ice sheet and apparent in Marie Byrd Land and near the Ross Embayment. Upper mantle low-velocity anomalies occur worldwide in regions that have undergone lithospheric rejuvenation [*Houseman and Molnar*, 2001] through extension since ~30 Ma. Many of these regions have Holocene volcanism. Examples include mid-oceanic ridges, back arc regions, and continental regions such as the Basin and Range, the East African Rift System, and eastern Turkey. As Figures 17a and 17b show, the characteristics of surface wave dispersion for the West Antarctic Rift differ sharply from mid-oceanic ridges and continental low-velocity features. Mid-ocean ridges are much faster at short periods because of thinner crust, and continental features are slower at all periods because of thicker crust and the absence of a lithospheric lid.

It is difficult for seismic evidence to either confirm or overturn the plume hypothesis because a plume neck may very well lie below the resolution of our model. However, the dispersion characteristics of the West Antarctic Rift are nearly indistinguishable from a number of regions, such as the western Mediterranean and certain marginal seas in the western Pacific, such as the Sea of Japan, as Figure 17a and 17b show. Figure 17c shows that the ensemble of acceptable models at the West Antarctic Rift is also consistent with the shear velocity structure underlying these regions, which have both undergone episodic extension with current quiescence. Therefore it is tempting to hypothesize by analogy that the low velocities underlying the West Antarctic Rift are the remnant of processes of lithospheric rejuvenation (e.g., extensional tectonics) during the Cenozoic that are now, for whatever reason, lying dormant.

4.3. Oceanic Lithosphere

The general characteristics of surface wave dispersion in oceanic regions, particularly the variation of intermediate- and

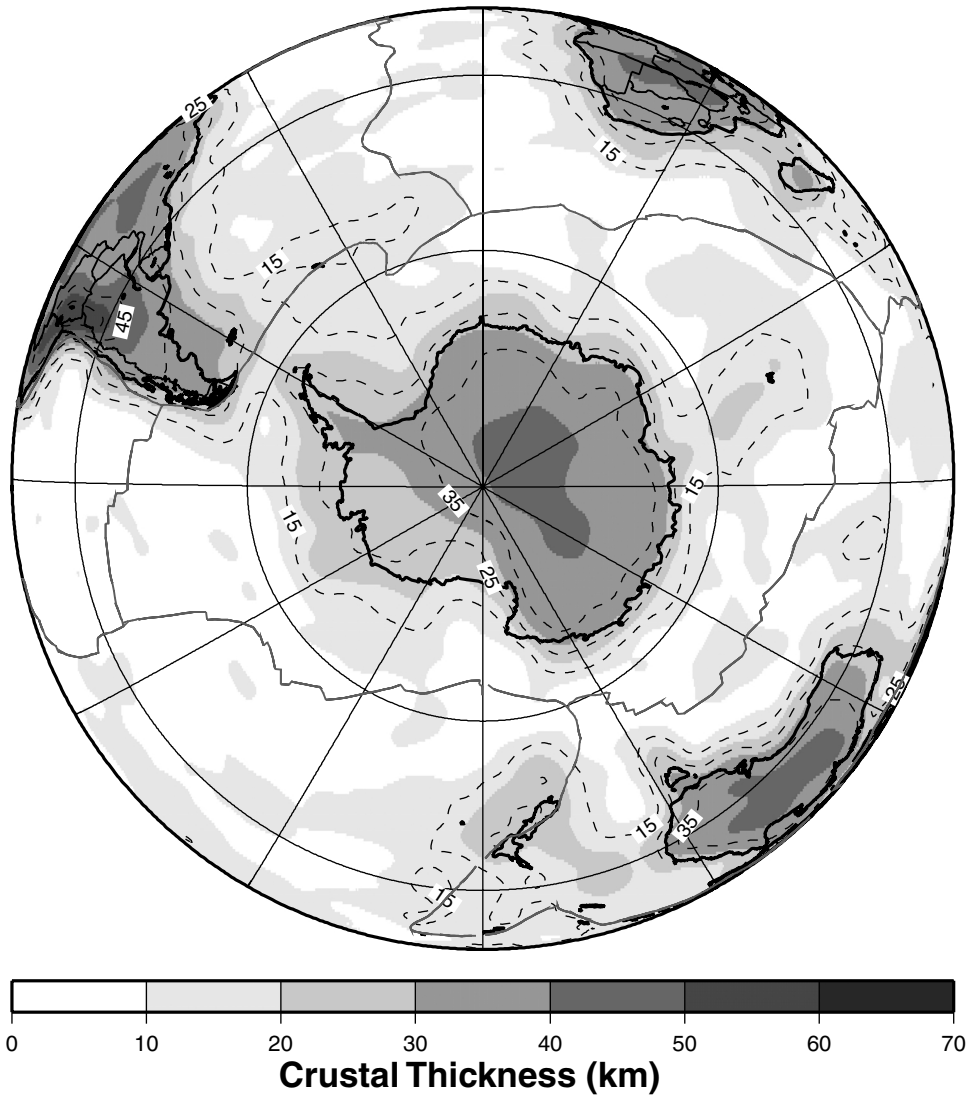

Figure 15. Crustal thickness, including ice thickness, from the median model. Dashed lines are at odd multiples of 5 km: 5, 15, 25 km, etc.

long-period phase velocities with lithospheric age, have been well documented, both globally [e.g., *Montagner and Tanimoto*, 1991; *Zhang and Tanimoto*, 1992, 1993; *Ekstrom and Dziewonski*, 1998] and regionally in the Southern Hemisphere [e.g., *Montagner and Jobert*, 1988; *Grad et al.*, 1993; *Silveira et al.*, 1998; *Vdovin*, 1999; *Vdovin et al.*, 1999; *Vuan et al.*, 1999]. On average, the oceanic lithosphere is characterized by a well-developed high-velocity lid overlying a prominent low-velocity zone (asthenosphere) with lithospheric lid thickness increasing with the age of the oceanic crust. The advantage of our study is the use of dispersion maps at periods shorter than 40 s, which helps to improve the resolution of the oceanic lithosphere from the asthenosphere. Plates 1 and 2 show that mid-ocean ridges do not begin to appear as low-velocity anomalies until periods of 40 s or so for group velocities. Thus, at shorter periods, which are dominantly sensitive to the oceanic lithosphere, oceanic dispersion characteristics are more homogeneous than at longer periods. One of the key motivations for providing more detailed models of the oceanic upper mantle is to resolve Richter-type convective rolls that may exist under the world's oceans [e.g., *Richter*, 1973; *Katzman et al.*, 1998]. Any inferences about convection patterns at high southern latitudes must await future work, however.

Figures 14b–14d show examples of the ensemble of acceptable models at three oceanic points. Figure 14 and Plate 4 indicate that as expected, ridges typically have low-velocity anomalies extending vertically up to the Moho, whereas ocean basins are characterized by a lithospheric lid that increases in thickness with lithospheric age. In addition, as Figure 14b and 14c show, ridges display weaker radial anisotropy than the ocean basins, as discussed further below. There are some anomalous regions along mid-ocean ridges, such as the Australian-Antarctic Discordance, which we also discuss further below. As Plate 4 shows, by a depth of 150 km, low-velocity anomalies prevail across the oceans of the Southern Hemisphere, characteristic of the asthenosphere. The asthenosphere can penetrate quite deeply in some places, such as the Bellingshausen Sea (Plate 5, C-C′). Unexpectedly, its maximum depth appears to rise under ridge crests, on average, so that mid-ocean ridges are underlain by high-velocity anomalies below 200–250 km. This feature may be caused by chemical heterogeneities that result from depleting the mantle in light

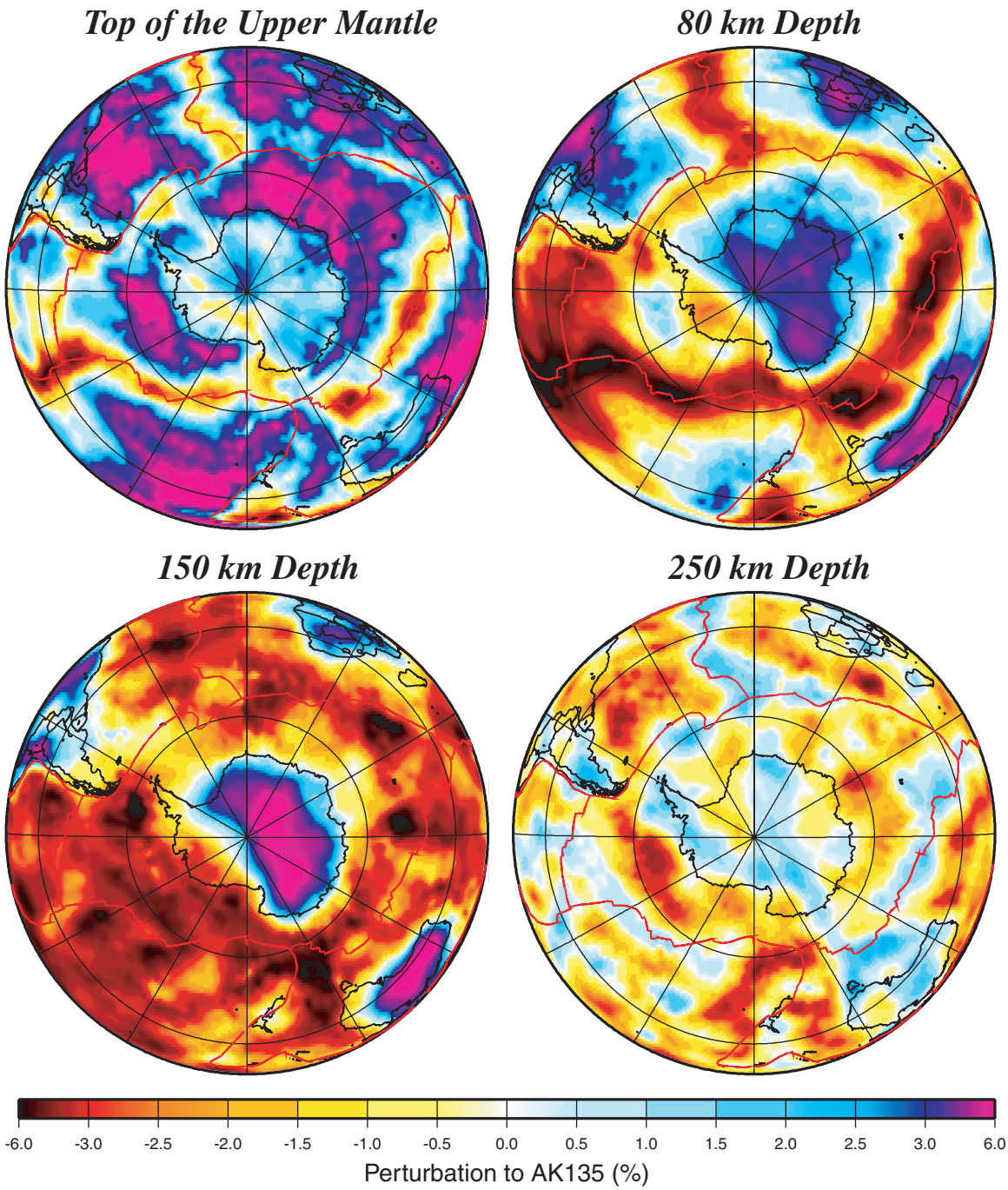

Plate 4. Horizontal slices of the median model at various depths. Isotropic shear velocity ($(v_{sh} + v_{sv})/2$) is percent relative to ak135.

elements under the ridges. In most regions this deep high-velocity anomaly is not a persistent feature of the median model, but it is persistent under some ridge segments such as the seismically very active East Australian–Antarctic Ridge (see Plate 5, slice A-A′). Further study is needed to establish confidence in this feature of the model.

4.4. Australian-Antarctic Discordance

The Australian-Antarctic Discordance (AAD) [*Weissel and Hayes*, 1971, 1974] is a portion of the Southeast Indian Ridge between about 120°E and 128°E characterized by a crenelated ridge pattern and a negative depth anomaly. The AAD is, in fact, the deepest segment of the world's mid-ocean ridge system and marks the boundary between Pacific and Indian type mid-ocean ridge basalts [*Klein et al.*, 1988]. It is believed that the AAD is a boundary between two different mantle provinces, with a magma deficit and thinner crust caused by cold upper mantle compared to adjacent ridge segments. Several models of the cause of the AAD have been proposed including the existence of a stable cold spot [*Hayes*, 1976]; convective downwelling [e.g., *Hayes*, 1988]; passive along-axis flow in response to colder temperatures along the ridge segment [e.g.,

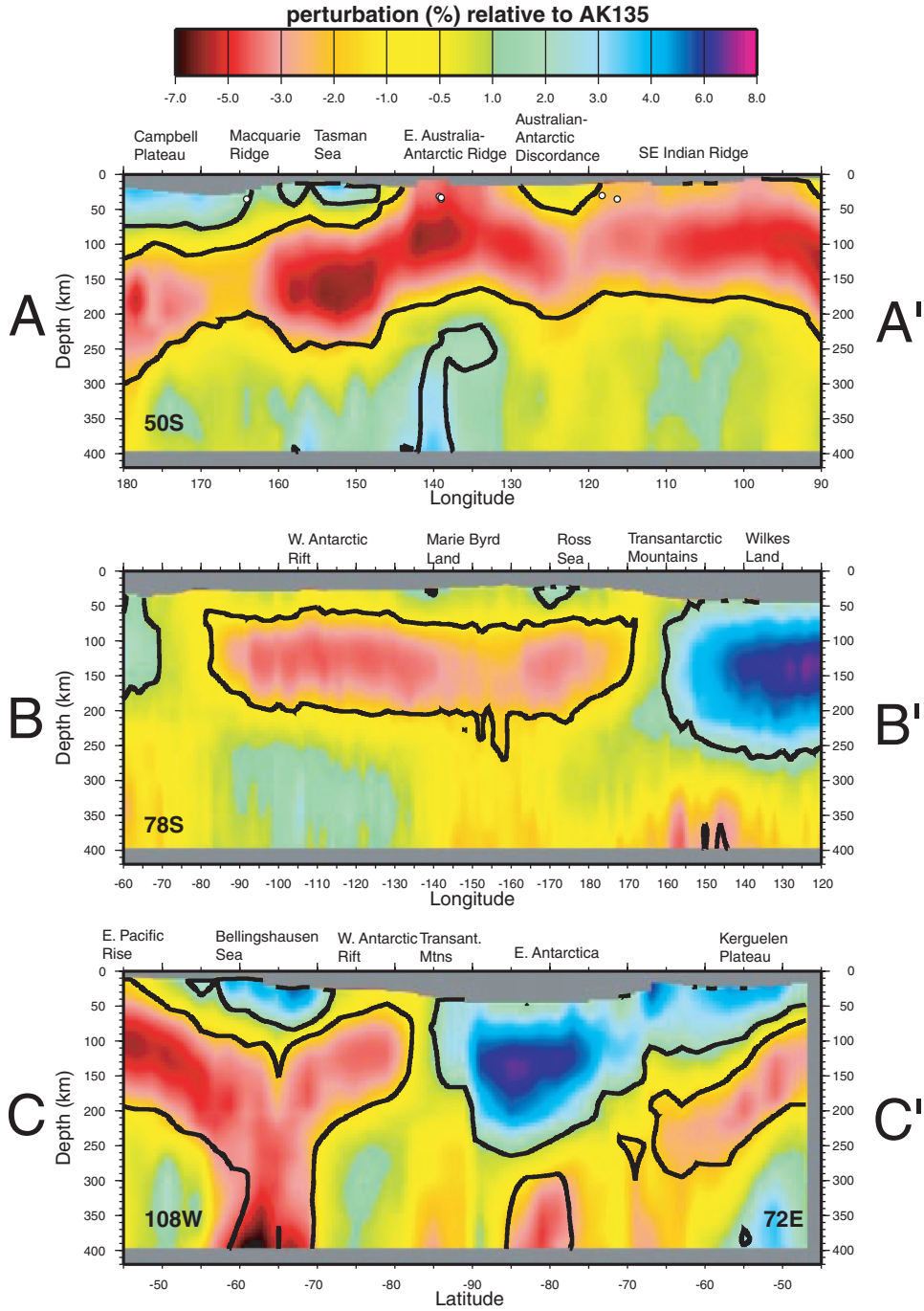

Plate 5. Vertical slices of the median model, along the three profiles (A-A′, B-B′, C-C′) indicated in Figure 1. The black contours outline the persistent features that appear in all members of the ensemble of acceptable models.

Forsyth et al., 1987; *West et al.*, 1997]; and the presence of a stagnated slab that subducted beneath the Gondwanaland-Pacific margin and subsequently has been drawn upward by the Southeast Indian Ridge beneath the AAD [*Gurnis et al.*, 1998]. *Marks et al.* [1999] present evidence that the causative process is continuing today.

Several studies of the AAD with surface wave dispersion have been previously performed [e.g., *Forsyth et al.*, 1987; *Kuo et al.*, 1996]. Our study contributes to this history by providing tomographic images of both surface wave dispersion and vertical profiles of the region around the AAD. Plate 1 shows that intermediate period (e.g., 45 s) Rayleigh wave group velocity maps image the AAD very well. The feature is observed as a high-velocity anomaly from ~35 s to 90 s with a northwest-southeast trend. In addition, a low-velocity anomaly appears to wrap around the AAD to its south. The AAD is not as unambiguously observed either on the Love wave group velocity maps or the phase velocity maps in Plates 2 and 3. At ~100 s period the Rayleigh wave group sensitivity kernels have appreciable amplitudes to depths of 100–150 km. The loss of the high-velocity

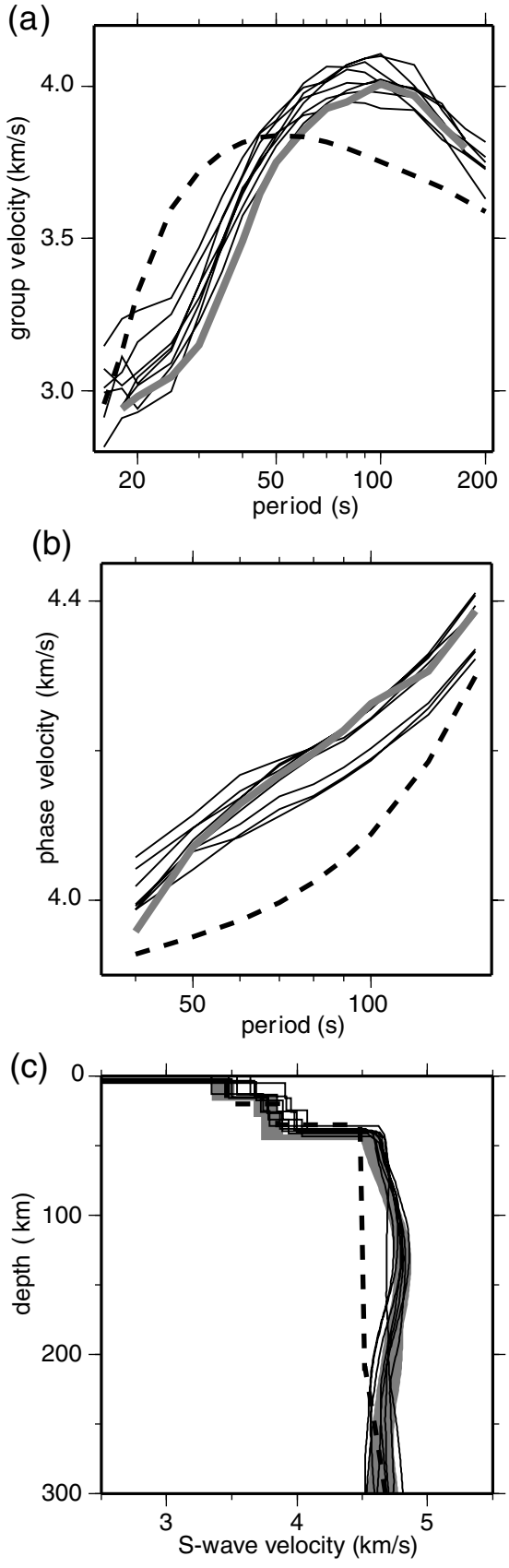

anomaly on the longer-period Rayleigh wave group velocity maps implies, therefore, that the relatively high velocity upper mantle structure beneath the AAD will be predominantly confined to depths above 100 km.

Figure 14d displays the ensemble of acceptable models near the middle of the AAD that show that the mantle underlying the AAD is intermediate between mid-ocean ridge and basin structures, typical examples of which are shown in Figures 14a–14c. The AAD is characterized by a lithospheric lid that has slower velocities than in ocean basins and by asthenosphere that is less prominent than along the rest of the Southeast Indian Ridge. The high-velocity lid is seen in Plates 4 and 5 (A-A′) to extend no deeper than ~70–80 km. At greater depths, more or less normal oceanic asthenosphere prevails, but there is a weak trend of relatively higher velocity material dipping to the west. Low-velocity material appears to wrap around to the south of the AAD in the upper mantle.

These observations confirm previous evidence of a low-temperature zone in the mantle but constrain the feature to lie predominantly above a depth of 70–80 km. The implication of the low velocities wrapping around to the south of the AAD in the upper mantle is not entirely clear, but it may hint at convective flows and perhaps incipient magma production to the south. The weak trend of high-velocity material dipping to the west of the AAD requires further data processing to resolve clearly. If it persists, it would be tempting to interpret it as a somewhat lower temperature zone that could either be the remnant of a primordial slab or the focus of shallow downwelling. Determining whether these interpretations make sense thermodynamically or geodynamically is beyond the scope of the present paper.

4.5. Radial Anisotropy

A transversely isotropic medium with vertical symmetry axis (radial anisotropy) is characterized by five mutually independent elastic moduli [*Smith and Dahlen*, 1973]: $A = \rho v_{ph}^2$, $C = \rho v_{pv}^2$, F, $L = \rho v_{sv}^2$, and $N = \rho v_{sh}^2$. Information about radial anisotropy worldwide derives mainly from observations of the Rayleigh-Love discrepancy [e.g., *Anderson*, 1961; *Cara et al.*, 1980; *James*, 1998]. Because Rayleigh and Love fundamental modes are nearly insensitive to v_p in the mantle, these waves constrain only two of the five moduli, L and N or v_{sv} and v_{sh}. The strength of radial anisotropy is frequently presented as $(v_{sh} - v_{sv})/v_{sv}$. Much effort has been devoted to estimating these quantities globally [e.g., *Dziewonski and Anderson*, 1981; *Montagner and Anderson*, 1989; *Montagner and Tanimoto*, 1991; *Ekstrom and Dziewonski*, 1998] and regionally in the Southern Hemisphere [e.g., *Montagner and Jobert*, 1988; *Villaseñor et al.*, 2001]. The groundwork for interpretation also has been laid [e.g., *Montagner*, 1994; *Babuska et al.*, 1998].

The robust estimation of v_{sv} and v_{sh}, especially on a regional scale, is much more difficult than estimating isotropic v_s. As an

Figure 16. (opposite) Fundamental Rayleigh wave dispersion and shear velocity for nine different cratons globally (SR2001): Canada, Brazil, north Greenland, West Africa, eastern Europe, Siberia, India, west Australia, and East Antarctica (Wilkes Land, 76°S, 120°E). (a) Group velocities extracted from the tomographic maps. (b) Phase velocities extracted from the tomographic maps. (c) Isotropic shear velocity ($v_s = (v_{sv} + v_{sh})/2$). In Figures 16a and 16b the dashed lines represent dispersion curves for PREM, and the thick shaded lines are for East Antarctica. In Figure 16c the dashed line is shear velocity for ak135, and the shaded corridor represents the ensemble of acceptable models at the East Antarctic location. The three slow group velocity curves in Figure 16b are for the smallest cratons (north Greenland, Brazil, India).

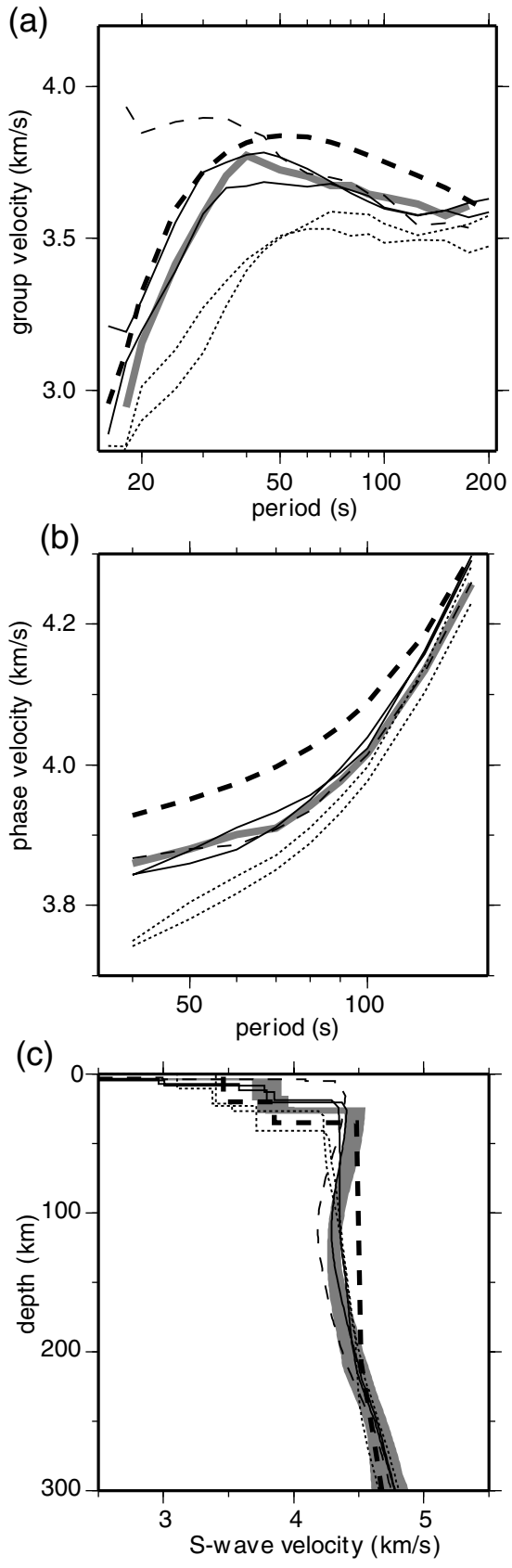

example, Figure 18 illustrates how the use of different subsets of our data set affects estimates of the strength of radial anisotropy. It is difficult to estimate the strength of radial anisotropy unambiguously using phase velocity measurements alone, and the joint use of phase and group velocity data is much better than applying either data set alone. In addition, SR2001 demonstrate that the estimated strength of radial anisotropy varies with allowable perturbations to v_p in the crust and with the parameterization of uppermost mantle v_s. We find that very simple parameterizations of the strength of radial anisotropy with depth can fit the group and phase velocity data simultaneously, as Figure 18 illustrates. More complicated vertical patterns of radial anisotropy are not resolvable with surface wave data alone.

Beneath Antarctica (Figure 19), as well as other regions worldwide [e.g., *Villaseñor et al.*, 2001], the strength of radial anisotropy averages ~4% in the uppermost mantle, similar to PREM. Almost everywhere v_{sh} is unambiguously faster than v_{sv}. It appears, however, that at mid-ocean ridges and subduction zones, radial anisotropy is weaker than beneath continents. This can be seen in the examples in Figures 14b, 14c, and 19. This presumably results from the fact that near mid-ocean ridges the preferred orientation of olivine crystals has not yet completely developed and near subduction zones the crystals that are aligned horizontally in ocean basins become tilted toward the vertical as the plate deforms. We see no evidence of the need for radial anisotropy much below ~225 km.

Estimation of the strength of radial anisotropy beneath Antarctica is particularly difficult because of the shortage of measurements of long-period Love waves, which is reflected in the path density and resolution maps (e.g., Figures 5, 6, and 8). Therefore, one needs to be cautious in interpreting variations in anisotropic characteristics across Antarctica. Radial anisotropy, however, appears to be slightly stronger in West Antarctica than in East Antarctica and in the thinner rather than in the thicker regions of the East Antarctic craton.

5. Conclusions

We believe that there are two characteristics of this study that set it apart from earlier studies. First, there is the data set. The simultaneous inversion of broadband group velocity measurements with intermediate- and long-period phase velocity measurements is much more powerful than the use of either data set alone. In continental regions the two data sets help to resolve the crust from the uppermost mantle, and in oceanic regions they improve the resolution of the lithosphere from the asthenosphere. These data sets also reduce ambiguities in estimating radial anisotropy in the uppermost mantle. The result is an improved model of the upper mantle. Second, there is the Monte Carlo inversion, which allows us to identify and focus interpretation on the more robust features of the model.

We have paid considerable attention to error analyses, in general. To summarize briefly, the median model ends up fitting the dispersion maps at about the measurement error (group velocities, 20–25 m/s; phase velocities, 10–15 m/s) and the dispersion data themselves at about twice the measurement error.

Figure 17. (opposite) Fundamental Rayleigh wave dispersion and shear velocity for six locations with low velocities in the uppermost mantle: Southeast Indian Ridge (thin dashed line), Sea of Japan and western Mediterranean (thin solid lines), eastern Turkey and Basin and Range (thin dotted lines), West Antarctic Rift (thick shaded line). Figures 17a, 17b, and 17c are defined as in Figure 16.

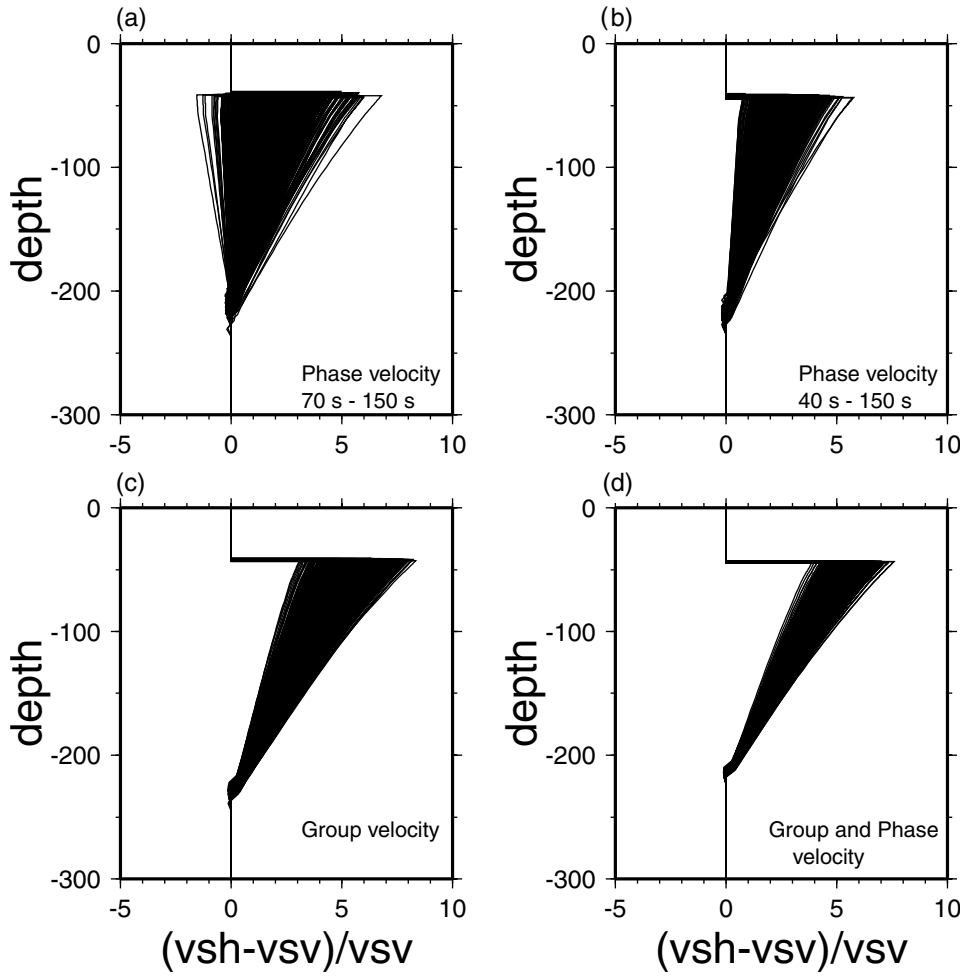

Figure 18. Demonstration of the ability of different data sets to estimate the strength of radial anisotropy for a point in East Antarctica (80°S, 90°E). Shown here are the full ensemble of 2000 acceptable models for each data set. (a) Use of only Rayleigh and Love phase velocities from 70 to 150 s to simulate inversions performed in the early to mid-1990s [e.g., *Montagner and Tanimoto*, 1991]. (b) The same as Figure 18a but using the full range of periods in this study, 40–150 s, to simulate more recent phase velocity inversions [e.g., *Ekstrom and Dziewonski*, 1998]. (c) Results using the Rayleigh and Love wave group velocities in this study to simulate recent studies with broadband group velocities alone [e.g., *Villaseñor et al.*, 2001]. (d) Results of combining the Rayleigh and Love wave group and phase velocities used in this study.

Some of the more robust, or "persistent," features of the model that are worthy of note are the following: (1) Crustal thickness averages ~27 km in West Antarctica and ~40 km in East Antarctica, with maximum thicknesses approaching 45 km. (2) Although the East Antarctic craton displays variations in both maximum velocity and thickness, it appears to be a more or less average craton. (3) Beneath much of West Antarctica the upper mantle is slow, and beneath the West Antarctic Rift it is nearly indistinguishable from currently dormant extensional areas such as the western Mediterranean and the Sea of Japan. The low velocities imply high temperatures. Our model therefore is consistent with evidence of active volcanism underlying the West Antarctic ice sheet, and we hypothesize that the West Antarctic Rift is the remnant of events of lithospheric rejuvenation in the Cenozoic that are now quiescent. These events may have included tectonic extension or the injection of a mantle plume, but the seismic evidence alone probably cannot distinguish between these competitors. (4) The Australian-Antarctic Discordance is characterized by a moderately high velocity lid to a depth of 70–80 km with low velocities wrapping around the discordance to the south. There is a weak trend of relatively high velocities dipping to the west at greater depths that requires further concentrated effort to resolve. (5) The strength of radial anisotropy $(v_{sh} - v_{sv})/v_{sv}$ in the uppermost mantle across the Southern Hemisphere averages ~4%, similar to PREM but considerably stronger than more recent estimates from models derived with phase velocity data alone [e.g., *Montagner and Tanimoto*, 1991]. Radial anisotropy appears to be slightly stronger in West Antarctica than in East Antarctica and in the thinner rather than the thicker regions of the East Antarctic craton.

Because of the poor distribution of seismicity and the shortage of receiving stations at high southern latitudes it is nearly certain that seismologists in the near future will continue to rely predominantly on surface wave dispersion to reveal information about the Antarctic crust and upper mantle. An exciting development that is now on the horizon is use of data from the

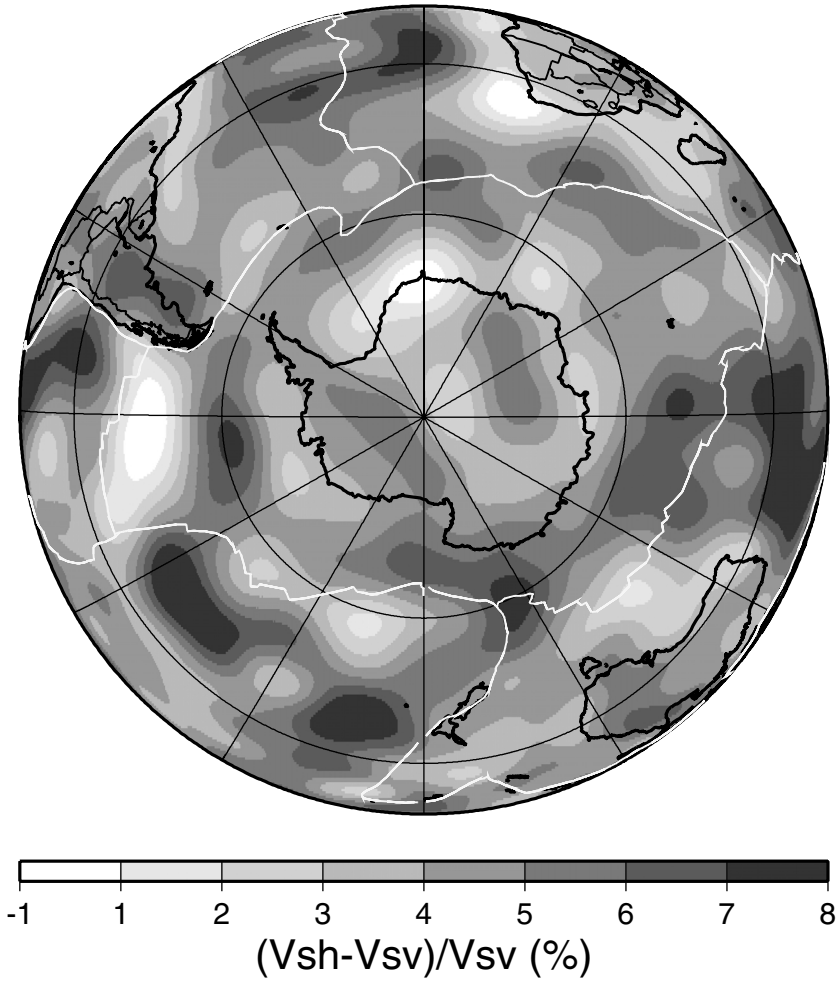

Figure 19. Strength of radial anisotropy at the top of the mantle in percent. For reference, PREM attains values of ~5% near the top of the mantle. White regions denote effectively isotropic regions.

broadband arrays of seismometers that have begun to appear in and around Antarctica, including, in greater numbers, installations on the ice [e.g., *Anandakrishnan et al.*, 2000]. We believe that the most noteworthy improvements in the understanding of the crust and upper mantle beneath Antarctica will probably result from these arrays.

Acknowledgments. We would like to thank Jeannot Trampert and two anonymous reviewers for insightful and helpful comments. We gratefully acknowledge the staffs at the IRIS-DMC and the Geoscope data center for providing most of the waveform data from which the dispersion measurements were obtained. We are also particularly grateful to Jeannot Trampert at Utrecht University and Michael Antolik and Goran Ekstrom at Harvard University for providing phase velocity measurements and to Robert van der Hilst and Brian Kennett for donating waveform data from the SKIPPY and KIMBA arrays in Australia. The SKIPPY and KIMBA data sets were collected by the Research School of Earth Sciences, Australian National University. Mikhail Barmin helped with the resolution analysis and Antonio Villaseñor converted the SKIPPY and KIMBA data into CSS3.0 format and oversaw the ordering and preprocessing of much of the waveform data. Several analysts contributed greatly to this project by expertly guiding the frequency-time measurement of group velocities; they include Lana Fedorova, William Landuyt, Ludmila Ratnikova, David Trembley, and Liz Zea. We would like to thank John Behrendt, Donald Blankenship, Ian Dalziel, and Peter Molnar for valuable conversations and tutoring. All maps were generated with the Generic Mapping Tools (GMT) data processing and display package [*Wessel and Smith*, 1991, 1995]. This work was supported by a grant from the Office of Polar Programs at the U.S. National Science Foundation, NSF-OPP-9615139.

References

Anandakrishnan, S., D. E. Voigt, P. Burkett, B. Long, and R. C. Henry, Deployment of a broad-band seismic network in West Antarctica, *Geophys. Res. Lett.*, *27*(14), 2053–2056, 2000.

Anderson, D. L., Elastic wave propagation in layered anisotropic media, *J. Geophys. Res.*, *66*, 2953–2963, 1961.

Babuska, V., J.-P. Montagner, J. Plomerova, and N. Girardin, Age-dependent large-scale fabric of the mantle lithosphere as derived from surface-wave velocity anisotropy, *Pure Appl. Geophys.*, *151*, 257–280, 1998.

Bannister, S., R. K. Snieder, and M. L. Passier, Shear-wave velocities under the Transantarctic Mountains and Terror Rift from surface wave inversion, *Geophys. Res. Lett.*, *27*(2), 281–284, 2000.

Barmin, M. P., A. L. Levshin, and M. H. Ritzwoller, A fast and reliable method for surface wave tomography, *Pure Appl. Geophys.*, *158*, 1351–1375, 2001.

Behrendt, J. C., W. E. LeMasurier, A. K. Cooper, T. Tessensohn, A. Trehu, and D. Damaske, Geophysical studies of the West Antarctic Rift system, *Tectonics*, *10*, 1257–1273, 1991.

Behrendt, J. C., W. E. LeMasurier, and A. K. Cooper, The West Antarctic rift system—A propagating rift "captured" by a mantle plume, in *Recent Progress in Antarctic Earth Science*, edited by K. Kaminuma and Y. Yoshida, pp. 315–322, Terra Sci., Tokyo, 1992.

Behrendt, J. C., D. D. Blankenship, C. A. Finn, R. E. Bell, R. E. Sweeney, S. M. Hodge, and J. M. Brozena, CASERTZ aero-magnetic data reveal late Cenozoic flood basalts in the West Antarctic Rift system, *Geology*, *22*, 527–530, 1994.

Behrendt, J. C., R. Saltus, D. Damaske, A. McCafferty, C. A. Finn, D. Blankenship, and R. E. Bell, Patterns of late Cenozoic volcanic and tectonic activity in the West Antarctic rift system revealed by aeromagnetic surveys, *Tectonics*, *15*, 660–676, 1996.

Bentley, C. R., Crustal structure of Antarctica from geophysical evidence — A review, in *Antarctic Earth Science*, edited by R. L. Oliver, P. R. James, and J. B. Jago, pp. 491–497, Aust. Acad. of Sci., Canberra, 1973.

Bentley, C. R., and N. A. Ostenso, On the paper of F. F. Evison, C. E. Ingram, R. H. Orr, and J. H. LeFort, Thickness of the Earth's crust in Antarctic and surrounding oceans, *Geophys. J. R. Astron. Soc.*, *6*, 292–298, 1962.

Blankenship, D. D., R. E. Bell, S. M. Hodge, J. M. Brozena, J. C. Behrendt, and C. A. Finn, Active volcanism beneath the West Antarctic ice sheet and implications for ice-sheet stability, *Nature*, *361*, 526–528, 1993.

Calcagnile, G., F. D'Ingeo, P. Farrugia, and G. F. Panza, The lithosphere in the central-eastern Mediterranean area, *Pure Appl. Geophys.*, *120*, 389–406, 1982.

Cande, S. C., J. M. Stock, R. D. Müller, and T. Ishihara, Cenozoic motion between East and West Antarctica, *Nature*, *404*, 145–150, 2000.

Cara, J., A. Nercessian, and G. Nolet, New inferences from higher mode data in western Europe and northern Eurasia, *Geophys. J. R. Astron. Soc.*, *61*, 459–478, 1980.

Christensen, N. I., and W. D. Mooney, Seismic velocity structure and composition of the continental crust: A global view, *J. Geophys. Res.*, *100*, 9761–9788, 1995.

Cooper, A. K., F. J. Davey, and G. R. Cochrane, Structure of extensionally rifted crust beneath the western Ross Sea and Iselin Bank, Antarctica, from sonobuoy seismic data, in *The Antarctic Continental Margin Geology and Geophysics of Western Ross Sea, Earth Sci. Ser.*, vol. 5B, edited by A. K. Cooper and F. J. Davey, pp. 27–76, Circum-Pac. Counc. for Energy and Nat. Resour., Houston, Tex., 1987.

Dahlen, F. A., and J. Tromp, *Theoretical and Global Seismology*, 1st ed., 1025 pp., Princeton Univ. Press, Princeton, N. J., 1998.

Danesi, S., and A. Morelli, Group velocity of Rayleigh waves in the Antarctic region, *Phys Earth Planet. inter.*, *122*, 55–66, 2000.

Dewart, G. M., and M. N. Toksoz, Crustal structure in East Antarctica from surface wave dispersion, *Geophys. J. R. Astron. Soc.*, *10*, 127–139, 1965.

DiVenere, V. J., D. V. Kent, and I. W. D. Dalziel, Mid-Cretaceous paleomagnetic results from Marie Byrd Land, West Antarctica: A test of post-100 Ma relative motion between East and West Antarctica, *J. Geophys. Res.*, *99*, 15,115–15,139, 1994.

Dziewonski, A. M., and D. L. Anderson, Preliminary Reference Earth Model, *Phys. Earth Planet. Inter.*, *25*, 297–356, 1981.

Ekstrom, G., and A. M. Dziewonski, The unique anisotropy of the Pacific upper mantle, *Nature*, *394*, 168–172, 1998.

Ekstrom, G., J. Tromp, and E. W. F. Larson, Measurements and global models of surface wave propagation, *J. Geophys. Res.*, *102*, 8137–8157, 1997.

Evison, F. F., Thickness of the Earth's crust in Antarctica and the surrounding oceans: A reply, *Geophys. J. R. Astron. Soc.*, *7*, 469–476, 1963.

Evison, F. F., C. E. Ingham, R. H. Orr, and J. H. LeFort, Thickness of the Earth's crust in Antarctica and the surrounding oceans, *Geophys. J. R. Astron. Soc.*, *3*, 289–306, 1960.

Forsyth, S. W., R. L. Ehrenbard, and S. Chapin, Anomalous upper mantle beneath the Australian-Antarctic discordance, *Earth Planet. Sci. Lett.*, *84*, 471–478, 1987.

Grad, M., A. Guterch, and T. Janik, Seismic structure of the lithosphere across the zone of subducted Drake plate under the Antarctic plate, West Antarctica, *Geophys. J. Int.*, *115*, 586–600, 1993.

Gurnis, M., R. D. Muller, and L. Moresi, Cretaceous vertical motion of Australia and the Australian-Antarctic Discordance, *Science*, *279*, 1499–1504, 1998.

Hayes, D. E., Nature and implications of asymmetric sea-floor spreading—Different rates for different plates, *Geol. Soc. Am. Bull.*, *87*, 994–1002, 1976.

Hayes, D. E., Age-depth relationships and depth anomalies in the southeast Indian Ocean and South Atlantic Ocean, *J. Geophys. Res.*, *93*, 2937–2954, 1988.

Hole, M. J., and W. E. LeMasurier, Tectonic controls on the geochemical composition of Cenozoic alkali basalts from West Antarctica, *Contrib. Mineral. Petrol.*, *117*, 187–202, 1994.

Houseman, G., and P. Molnar, Continental Reactivation and Reworking, *Geol. Soc. Spec. Publ.*, *184*, 13–37, 2001.

Ingber, L., Very fast simulated re-annealing, *J. Math. Comput. Model.*, *12*, 967–973, 1989.

Ito, K., and A. Ikami, Crustal structure of the Mizuho Plateau, East Antarctica, from geophysical data, *J. Geodyn.*, *6*, 285–296, 1986.

James, M. B., On the discrepancy between long period Rayleigh and Love wave data in continental regions, M.S. thesis, 87 pp., Univ. of Colo., Boulder, May 1998.

James, M. B., and M. H. Ritzwoller, Feasibility of truncated perturbation expansions to approximate Rayleigh wave eigenfrequencies and eigenfunctions in heterogeneous media, *Bull. Seismol. Soc. Am.*, *89*, 433–442, 1999.

Jaupart, C., J. C. Mareschal, L. Guillo-Frottier, and A. Davaille, Heat flow and the thickness of the lithosphere in the Canadian Shield, *J. Geophys. Res.*, *103*, 15,269–15,286, 1998.

Katzman, R., L. Zhao, and T. H. Jordan, High-resolution, two-dimensional vertical tomography of the central Pacific mantle using *ScS* reverberations and frequency-dependent travel times, *J. Geophys. Res.*, *103*, 17,933–17,971, 1998.

Keen, C. E., R. C. Courtney, S. A. Dehler, and M.-C. Williamson, Decompression melting at rifted margins: Comparison of model predictions with the distribution of igneous rocks on the eastern Canadian margin, *Earth Planet Sci. Lett.*, *121*, 403–416, 1994.

Keilis-Borok, V. I., and T. B. Yanovskaya, Inverse problems in seismology (structural review), *Geophys. J. R. Astron. Soc.*, *13*, 223–234, 1967.

Kennett, B. L. N., E. R. Engdahl, and R. Buland, Constraints on seismic velocities in the Earth from travel times, *Geophys. J. Int.*, *122*, 108–124, 1995.

Kiele, J., D. L. Marshall, P. R. Kyle, K. Kaminuma, K. Shibuya, and R. R. Dibble, Volcanic activity associated and seismicity of Mount Erebus, 1982–1983, *Antarct. J. U.S.*, *18*, 41–44, 1983.

Kirkpatrik, S., C. D. Gellat, and M. P. Vecchi, Optimisation by simulated annealing, *Science*, *220*, 671–680, 1983.

Klein, E. M., C. H. Langmuir, A. Zindler, H. Staudigel, and B. Hamelin, Isotope evidence of a mantle convection boundary at the Australian-Antarctic Discordance, *Nature*, *333*, 623–629, 1988.

Knopoff, L., and G. Vane, Age of East Antarctica from surface wave dispersion, *Pure Appl. Geophys.*, *117*, 806–816, 1978.

Kogan, A. L., Results of deep seismic soundings of the earth's crust in East Antarctica, in *Antarctic Geology and Geophysics*, edited by R. J. Adie, pp. 485–489, Universitetsforlaget, Oslo, 1972.

Kovach, R. L., and F. Press, Surface wave dispersion and crustal structure in Antarctica and the surrounding oceans, *Ann. Geofis.*, *14*, 211–224, 1961.

Kuo, B.-Y., C.-H. Chen, and Y.-S. Zhang, A fast anomaly to the west of the Australian-Antarctic Discordance, *Geophys. Res. lett.*, *23*, 2239–2242, 1996.

LeMasurier, W. E., Late Cenozoic volcanism on the Antarctic Plate — An overview, in *Volcanos of the Antarctic Plate and Southern Oceans, Antarct. Res. Ser.*, vol. 48, edited by W. E. LeMasurier and J. W. Thompson, pp. 1–11, AGU, Washington, D. C., 1989.

Levshin, A. L., T. M. Sabitova, and V. P. Valus, Joint interpretation of body and surface waves data for a district in Middle Asia, *Geophys. J. R. Astron. Soc.*, *11*, 57–66, 1966.

Levshin, A. L., M. H. Ritzwoller, and J. S. Resovsky, Source effects on surface wave group travel times and group velocity maps, *Phys. Earth Planet. Inter.*, *115*, 293–312, 1999.

Levshin, A. L., M. H. Ritzwoller, M. P. Barmin, and A. Villaseñor, New constraints on the Arctic crust and uppermost mantle: Surface wave group velocities P_n, and S_n, *Phys. Earth Planet. Inter.*, *123*, 185–204, 2001.

Lomax, A., and R. Snieder, Finding sets of acceptable solutions with a genetic algorithm with application to surface wave group velocity dispersion in Europe, *Geophys. Res. Lett.*, *21*, 2617–2620, 1994.

Luyendyk, B., S. Cisowski, C. Smith, S. Richard, and D. Kimbrough, Paleomagnetic study of the northern Ford Ranges, western Marie Byrd Land, West Antarctica: Motion between West and East Antarctica, *Tectonics*, *15*, 122–141, 1996.

Marks, K. M., J. M. Stock, and K. J. Quinn, Evolution of the Australian-Antarctic discordance since Miocene time, *J. Geophys. Res.*, *104*, 4967–4981, 1999.

Masters, G., S. Johnson, G. Laske, and H. Bolton, A shear velocity model of the mantle, *Philos. Trans. R. Soc. London, Ser. A*, *354*, 1385–1411, 1996.

Meissner, R., *The Continental Crust*, Academic, San Diego, Calif., 1986.

Montagner, J.-P., Can seismology tell us anything about convection in the mantle?, *Rev. Geophys.*, *32*, 115–137, 1994.

Montagner, J.-P., and D. L. Anderson, Constrained reference mantle model, *Phys. Earth Planet. Inter.*, *58*, 205–227, 1989.

Montagner, J.-P., and N. Jobert, Vectorial tomography, II, Application to the Indian Ocean, *Geophys. J.R. Astron. Soc.*, *94*, 309–344, 1988.

Montagner, J.-P., and T. Tanimoto, Global upper mantle tomography of seismic velocities and anisotropies, *J. Geophys. Res.*, *96*, 20,337–30,351, 1991.

Mooney, W. D., G. Laske, and G. Masters, CRUST5.1: A global model at 5 degrees by 5 degrees, *J. Geophys. Res.*, *102*, 727–748, 1998.

Neunhofer, H., A. Frischbutter, and D. Guth, Contribution to Rayleigh wave dispersion in Antarctica and comparison to eastern Europe, *Gerlands Beitr. Geophys.*, *95*(5), 428–434, 1983.

Okal, E. A., Intraplate seismicity of Antarctica and tectonic implications, *Earth Planet. Sci. Lett.*, *52*, 397–409, 1981.

Press, F., Earth models obtained by Monte Carlo inversion, *J. Geophys. Res.*, *67*, 1647–1658, 1968.
Richter, F., Convection and large-scale circulation of the mantle, *J. Geophys. Res.*, *78*, 6783–6795, 1973.
Ritzwoller, M. H., and A. L. Levshin, Eurasian surface wave tomography: Group velocities, *J. Geophys. Res.*, *103*, 4839–4878, 1998.
Rodi, W. L., P. Glover, T. M. C. Li, and S. S. Alexander, A fast, accurate method for computing group-velocity partial derivatives for Rayleigh and Love modes, *Bull Seismol. Soc. Am.*, *65*, 1105–1114, 1975.
Rouland, D., S. H. Xu, and F. Schindele, Upper mantle structure in the southeast Indian Ocean: A surface wave investigation, *Tectonophysics*, *114*, 281–292, 1985.
Roult, G., and D. Rouland, Antarctica, I, Deep structure investigations inferred from seismology: A review, *Phys. Earth Planet. Inter.*, *84*, 15–32, 1994.
Roult, G., D. Rouland, and J. P. Montagner, Antarctica II: Upper mantle structure from velocities and anisotropy, *Phys. Earth Planet. Inter.*, *84*, 33–57, 1994.
Shapiro, N. M., M. Campillo, A. Paul, S. K. Singh, D. Jongmans, and F. J. Sanchez-Sesma, Surface wave propagation across the Mexican Volcanic Belt and the origin of the long-period sesimic wave amplification in the valley of Mexico, *Geophys. J. Int.*, *128*, 151–166, 1997.
Silveira, G., E. Stutzmann, J.-P. Montagner, and L. Mendes-Victor, Anisotropic tomography of the Atlantic Ocean from Rayleigh surface waves, *Phys. Earth Planet. Inter.*, *106*, 259–275, 1998.
Smith, M. L., and F. A. Dahlen, The azimuthal dependence of Love- and Rayleigh-wave propagation in a slightly anisotropic medium, *J. Geophys. Res.*, *78*, 3321–3333, 1973.
Trampert, J., and J. Woodhouse, Global phase velocity maps of Love and Rayleigh waves between 40 and 150 seconds, *Geophys. J. Int.*, *122*, 675–690, 1995.
Vdovin, O. Y., Surface wave tomography of South America and Antarctica, Ph.D. thesis, 131 pp., Univ. of Colo., Boulder, May 1999.
Vdovin, O., J. A. Rial, A. L. Levshin, and M. H. Ritzwoller, Group-velocity tomography of South America and the surrounding oceans, *Geophys. J. Int.*, *136*, 324–340, 1999.
Villaseñor, A., M. H. Ritzwoller, A. L. Levshin, M. P. Barmin, E. R. Engdahl, W. Spakman, and J. Trampert, Shear velocity structure of Central Eurasia from inversion of surface wave velocities, *Phys. Earth Planet. Inter.*, *123*, 169–184, 2001.
Vuan, A., R. Cazzaro, G. Costa, M. Russi, and G. F. Panza, S-wave velocity models in the Scotia Sea region, Antarctica, from non-linear inversion of Rayleigh wave dispersion, *Pure Appl. Geophys.*, *154*(1), 121–139, 1999.
Weissel, J. K., and D. E. Hayes, Asymmetric spreading south of Australia, *Nature*, *213*, 518–521, 1971.
Weissel, J. K., and D. E. Hayes, The Australian-Antarctic Discordance: New results and implications, *J. Geophys.*, *79*, 2579–2587, 1974.
Wessel, P., and W. H. F. Smith, Free software helps map and display data, *Eos. Trans. AGU*, *72*, 441, 445–446, 1991.
Wessel, P., and W. H. F. Smith, New version of the Generic Mapping Tools released, *Eos. Trans. AGU*, *76*, 329, 1995.
West, B. P., W. S. D. Wilcock, and J.-C. Sempere, Three-dimensional structure of asthenospheric flow beneath the Southeast Indian Ridge, *J. Geophys. Res.*, *102*, 7783–7802, 1997.
Woodhouse, J. H., The calculation of the eigenfrequencies and eigenfunctions of the free oscillations of the Earth and the Sun, in *Seismological Algorithms*, edited by D. J. Doornbos, pp. 321–370, Academic, San Diego, Calif., 1988.
Zhang, Y. S., and T. Tanimoto, Ridges, hotspots, and their interaction as observed in seismic velocity maps, *Nature*, *355*, 45–49, 1992.
Zhang, Y. S., and T. Tanimoto, High-resolution global upper mantle structure and plate tectonics, *J. Geophys. Res.*, *98*, 9793–9823, 1993.

G. M. Leahy, A. L. Levshin, M. H. Ritzwoller, and N. M. Shapiro, Center for Imaging the Earth's Interior, Department of Physics, University of Colorado, Campus Box 390, Boulder, CO 80309-0390, USA. (leahyg@ciei.colorado.edu; levshin@ciei.colorado.edu; ritzwoller@ciei.colorado.edu; nshapiro@ciei.colorado.edu)

(Received January 24, 2001; revised June 8, 2001;
accepted June 9, 2001.)